

Constitution and Structure of Earth's Mantle: Insights from Mineral Physics and Seismology

Andrea Zunino,¹ Amir Khan,² Paul Cupillard,³ and Klaus Mosegaard¹

ABSTRACT

Geophysical, geochemical, and petrological methods have played prominent roles in determining constitution and structure of the Earth. Most of Earth's interior remains geochemically unsampled, however, and direct measurements or numerical simulations of physical properties (e.g., elasticity and density) of natural samples and analogs at the physical conditions of the deep Earth allow us to compare with properties obtained from geophysical field models. These sources constitute a large complement of information that helps constrain possible models of Earth's mantle (and core) composition, temperature, and mineralogy. Traditionally, therefore, inference has proceeded by way of estimating "laboratory-based" profiles of physical properties with the intent of comparing these with field-derived estimates. A more definitive approach, however, resides in integrating data and results from experimental measurements, theoretical considerations, and inverse calculations to directly transform geophysical data into the main parameters of interest. In this study, we describe a quantitative approach that integrates data and results from mineral physics, petrological analyses, and geophysical inverse calculations to map geophysical data directly for mantle composition and thermal state. Computation of physical properties using thermodynamic models is described and discussed, and an application of the joint inverse methodology is illustrated in a case study where mantle composition and thermal state beneath continental Australia is determined directly from seismic data.

11.1. INTRODUCTION

Seismic tomography has proved an important tool to image the inaccessible parts of the Earth and has done much to enhance our understanding of deep-Earth processes and their relation to surface geology. For example, upper mantle seismic wave-speed variations at the global and regional scales are observed to correlate strongly

with tectonic features. Tectonically old and stable lithosphere shows up in the form of fast seismic wave speeds, whereas regions that have undergone relatively recent tectonic activity are distinguished by slow wave speeds (e.g., see *Fichtner et al.* [2010], *Khan et al.* [2011], *Lekic and Romanowicz* [2011], and *Schaeffer and Lebedev* [2013]). This suggests that lateral variations in the upper mantle are temperature-dominated [e.g., see *Goes et al.* [2000]]. But what is the contribution of compositional variations to Earth's present-day structure? Since entities such as temperature and composition ultimately reflect internal processes related to Earth's current state and past dynamics and, hence, its origin and evolution, unraveling Earth's chemical make-up and thermal state is of fundamental

¹*Solid Earth Physics, Niels Bohr Institute, University of Copenhagen, Copenhagen, Denmark*

²*Institute of Geophysics, Swiss Federal Institute of Technology, Zürich, Switzerland*

³*Laboratoire GeoRessources, Université de Lorraine, CNRS, Vandœuvre-lès-Nancy, France*

importance to Earth science (e.g., see *van der Hilst et al.* [2005], *Karato* [2013], and *Khan and Deschamps* [2015]).

In the absence of samples and in situ measurements, geophysical methods (based on, for example, seismology) are insufficient because these can only provide clues about the main parameters of interest (temperature and composition). So, how can we determine these quantities from measurements made at Earth's surface? Since we lack analytical expressions describing the temperature-dependent constitutive relations between stress, strain, and strain rate that are needed to compute the physical properties as functions of pressure and temperature, we rely on the use of thermodynamical theory. This, supplemented with mineral physics data, presents the principal means of establishing a link between geophysical observables and the fundamental thermochemical parameters of interest. As reviewed elsewhere (e.g., see *Stixrude and Jeanloz* [2007]), the main aim of mineral physics is the use of high-pressure devices and computer simulations based on first-principles theory to measure or determine properties of Earth materials at conditions of the deep Earth to help constrain the aforementioned constitutive relations. By comparing the elastic properties measured in the laboratory and computed numerically with those determined seismologically, we are able to place observational constraints on the interior structure. This approach is illustrated with the method of Adams and Williamson, who used seismically determined bulk sound velocity and compressibility measurements to show that Earth is well-approximated by a set of adiabatic and homogeneous layers (e.g., see *Anderson* [1989]).

The remarkable growth—both in quantity and quality—of high-pressure and high-temperature (high P–T) measurements of thermodynamic properties of crust and mantle materials (e.g., see *Holland and Powell* [1998] and *Stixrude and Lithgow-Bertelloni* [2005a, 2011]) has enabled quantitative inferences on the distribution of temperature and composition to be made. Methods employed for this purpose are generally classifiable in terms of forward and inverse approaches. An additional subclassification describes the particular observation used to calculate the “misfit” measure—that is, whether geophysical models or proper geophysical data are employed as a means of achieving model improvement. As an example of the simplified forward modeling approach, where a small number of models are tested for consistency with real data, we would compute, based on a parameterized phase-diagram approach (i.e., fixed composition and geotherm) seismic wave speeds, for example, and compare these to radial profiles of Earth's structure (e.g., see *Jackson* [1998], *Vacher et al.* [1998], *da Silva et al.* [2000], *Goes et al.* [2000], *Deschamps et al.* [2001], *Marton and Cohen* [2002], *Cammarano et al.* [2003], *Stixrude*

and *Lithgow-Bertelloni* [2005a], *Xu et al.* [2008], and *Kuskov et al.* [2011, 2014]) or globally averaged geophysical observables such as travel times, normal modes, and electromagnetic sounding data (e.g., see *Dobson and Brodholt* [2000], *Xu et al.* [2000], *Cammarano et al.* [2005, 2009], and *Fullea et al.* [2011]). Inverse approaches, on the other hand, tend to be more sophisticated in that geophysical datasets are directly inverted for one-dimensional radial profiles or three-dimensional grids of bulk composition and temperature. Given the complexity and nonuniqueness of the problem, the latter approach clearly presents a more appropriate means of analysis and includes studies that focus both on radial variations (e.g., see *Mattern et al.* [2005], *Khan et al.* [2006], *Matas et al.* [2007], *Cobden et al.* [2008], and *Verhoeven et al.* [2009]) and analysis of lateral distributions of temperature and composition on both regional and global scales (e.g., see *Shapiro and Ritzwoller* [2004], *Trampert et al.* [2004], and *Khan et al.* [2009], *Ritsema et al.* [2009], *Simmons et al.* [2010], *Cammarano et al.* [2011], *Khan et al.* [2011], *Fullea et al.* [2012], *Mosca et al.* [2012], *Afonso et al.* [2013a,b], *Drilleau et al.* [2013], *Khan et al.* [2013], and *Kaban et al.* [2014]).

These studies provide considerable evidence for the presence of thermochemical variations in the mantle. Although thermal variations tend to govern the physical structure of the lithosphere and upper mantle as shown in many studies (e.g., see *Shapiro and Ritzwoller* [2004], *van Gerven et al.* [2004], *Goes et al.* [2005], *Schuberth et al.* [2012], and *Kaban et al.* [2014]), compositional effects cannot be excluded even at long wavelengths (e.g., see *Khan et al.* [2013]). Moreover, transition zone structure appears to be complex and decoupled from that of the upper mantle, raising the question of what physical processes or mechanisms are responsible for producing the imaged lateral wave-speed variations (e.g., see *Lee et al.* [2014], *Takeuchi et al.* [2014], *Schmandt et al.* [2014], *Emry et al.* [2015], *Koyama et al.* [2014], and *Thompson et al.* [2015]) and their relation, if any, to mantle dynamics. In this context, the internal dynamics of the Earth are driven by lateral density variations (e.g., see *Forte and Perry* [2000] and *Deschamps et al.* [2001]). Yet, while detailed maps of compressional and shear-wave velocity models exist, there are few constraints on mantle density structure (e.g., see *Kennett et al.* [1998] and *Ishii and Tromp* [2004]), because of the relative insensitivity of seismic data to density (e.g., see *Resovsky and Ritzwoller* [1999], *Romanowicz* [2001], and *Kuo and Romanowicz* [2002]).

Thus, it is our contention that in order to improve our understanding of the observed complexity, it is desirable to invert directly for thermal state and composition of Earth's interior using a multiparameter inversion scheme as laid out in, for example, *Khan et al.* [2009]. There are

several advantages to this approach: (1) We address the fundamental parameters of interest; (2) we enable joint inversion of different geophysical datasets (e.g., seismic, electromagnetic, and gravity) and are able to simultaneously constrain P-wave speed, S-wave speed, and density; (3) we can integrate information and/or data from other disciplines (e.g., petrology); and (4) we implicitly take into account structure associated with thermochemically induced mineralogical phase transitions as observed in the laboratory.

The multiparameter joint inversion scheme makes use of a self-consistent thermodynamic methodology in the form of Gibbs free-energy minimization. Gibbs energy minimization is a technique by which rock mineralogy, and ultimately its elastic properties, can be predicted as a function of pressure, temperature, and bulk composition from thermodynamic data (e.g., *Connolly* [2005, 2009]). Although Gibbs energy minimization has long been advocated for geophysical problems (e.g., see *Saxena and Eriksson* [1983], *Wood and Holloway* [1984], *Kuskov and Panferov* [1991], *Sobolev and Babeyko* [1994], *Bina* [1998], and *Fabrichnaya* [1999]), it is only in the last decade that the availability of comprehensive thermodynamic databases (e.g., see *Ricard et al.* [2005], *Stixrude and Lithgow-Bertelloni* [2005b], *Khan et al.* [2006], *Piazzoni et al.* [2007], and *Stixrude and Lithgow-Bertelloni* [2011]) has made the application of such calculations feasible for geophysical models of Earth's entire mantle.

In the following, we describe a strategy to determine composition and thermal state of Earth's mantle directly from inversion of geophysical data. The theoretical framework we rely on is based on the probabilistic approach to inverse problems, which provides the tools to integrate information from different sources in a consistent algorithm as outlined in more detail by *Mosegaard and Hansen* [2016], *Bosch* [2016], and *Hansen et al.* [2016] (Chapters 2, 3, and 6 *this volume*). While our approach will be that of the inverse problem, we illustrate and discuss the connection between temperature, composition, mineral properties, resultant Earth structure, and seismic data. As an inverse application we discuss results from inversion of surface-wave phase-velocity data [*Khan et al.*, 2013] for thermochemical structure of the mantle beneath continental Australia. As an example of posterior filtering (e.g., see *Khan et al.* [2011]), we compute full waveform synthetics for a set of solution models and compare these to observed waveforms from selected seismic stations across Australia. Finally, the study of *Afonso et al.* [2016] (Chapter 10, *this volume*) presents a complementary study to this contribution and emphasizes the growing popularity of integrated studies.

11.2. THE FORWARD PROBLEM: FROM THERMO-CHEMICAL MODELS TO SEISMIC DATA

The study of Earth's deep interior is highly challenging because of our inability to directly probe the Earth by exploration and lack of representative samples for most of the deep Earth. Instead, models of the interior rely entirely on theory and laboratory measurements performed on mineral analogs. Comparison of these laboratory-based models with radial profiles of seismic wave speeds (e.g., PREM, AK135) or tomographic images, for example, enables qualitative understanding to be gained. This is illustrated in the approach of *Birch*, who used mostly experimental shock-wave data and compared these to seismological models of the day. This led to the recognition that seismic discontinuities are most likely related to the transformation of major minerals—for example, the transformation of olivine to its high-pressure phases [*Birch*, 1952]. This type of procedure for estimating constitution and structure of the Earth, although more advanced now, is still practiced. Most attempts rely on a two-step “inversion” procedure: Smooth velocity models resulting from linearized seismic tomography are “converted” to properties of interest, typically temperature, using parameterized phase-diagram approaches. However, from a thermodynamic perspective, such a procedure is not self-consistent, because physical properties and phase equilibria are derived independently. As a consequence, physical properties will not satisfy fundamental thermodynamic relations, which can lead to inconsistencies (e.g., see *Cammarrano et al.* [2003], *Hacker et al.* [2003], *Goes et al.* [2004], *Shapiro and Ritzwoller* [2004], and *Trampert et al.* [2004]).

Since our aim here is to compute geophysical data (e.g., seismic waveforms) from arbitrary models of Earth's mantle composition and thermal state and to compare these quantitatively with observations, a more general framework is required to properly reconcile the various aspects involved. Our strategy is to develop a sequential algorithm that computes, based on a mineral physics database (compilation of experimental and theoretical results for thermodynamic properties of mantle minerals), the stable mineral modes and their physical properties. These are subsequently employed as input for seismic waveform modeling and comparison to observations. This sequential approach ensures that the data computed are consistent with theory, laboratory-data, and any other information needed in the process.

Figure 11.1 illustrates schematically the various steps involved in the procedure outlined above. The first step involves computing the stable minerals, their proportions, and properties as a function of temperature, pressure, and chemical composition. The second step consists in

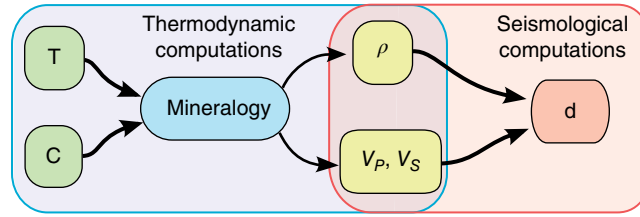


Figure 11.1 Illustration of the joint geophysical–thermodynamic forward problem for computing seismic data from thermochemical parameters (C , T). Mineralogy refers to modal mineralogy and physical properties include density (ρ) and isotropic P- and S-wave speeds (V_p and V_s).

computing bulk rock properties from properties of single minerals through use of the theory of composites. Finally, in the third step, seismic waves, for example, are propagated through the (an)elastic model obtained in steps 1 and 2 to compute seismograms at selected locations on the surface. Although we concentrate on seismology and full-waveform solvers, geophysical data from other disciplines such as gravity and electromagnetic sounding could easily be employed [Verhoeven *et al.*, 2009; Cammarano *et al.*, 2011; Khan *et al.*, 2011, 2013; Fullea *et al.*, 2012; Khan and Shankland, 2012; Afonso *et al.*, 2013a,b; Kaban *et al.*, 2014].

11.2.1. Thermodynamics of Mantle Minerals

11.2.1.1. Mantle Compositional Models

Recycling of subducted lithospheric material that originates from differentiation and melting of mantle peridotites at mid-ocean ridges (producing a basaltic crust overlying a depleted an olivine-rich residuum, harzburgite) is believed to be the major mechanism responsible for the production and maintenance of mantle heterogeneities [Hofmann, 1997; Helffrich and Wood, 2001; Tackley *et al.*, 2005; Anderson, 2007]. Based on this compositional end-member model, Xu *et al.* [2008] proposed a simple parameterization to investigate the effect of composition and temperature on seismic properties of the mantle. Mantle composition was parameterized in terms of a single depth-dependent variable that represents the weight fraction of basalt in a basalt-harzburgite mixture. In addition, Xu *et al.* [2008] considered two physical models for defining the “make-up” of the mantle: (1) equilibrium assemblage (EA) and (2) mechanical mixture (MM). In the EA model, the mantle is assumed to have reached chemical equilibrium, whereas in the MM model the bulk rock is composed of a solid–solid mixture of the two end-members.

With the above definitions, phase assemblages for the two models are given by

$$\text{EA} : \Phi [CX_B + (1-C)X_H] \quad (11.1)$$

Table 11.1 Model End-Member Bulk Compositions in Weight Percent^a

Oxide	Basalt (X_B)	Harzburgite (X_H)
Na ₂ O	1.87	0.01
CaO	13.05	0.50
FeO	7.68	7.83
MgO	10.49	46.36
Al ₂ O ₃	16.08	0.65
SiO ₂	50.39	43.64

^a Basalt and harzburgite compositions are taken from Khan *et al.* [2009].

and

$$\text{MM} : C\Phi[X_B] + (1-C)\Phi[X_H], \quad (11.2)$$

where Φ represents the vector of phase proportions, X_C the vector defining basalt and harzburgite compositions, respectively, and C the basalt fraction (ranging from 0 to 1). In the equilibrium model the properties of interest are calculated from the stable mineralogy for a given composition, whereas in the mechanical mixing model the bulk properties of the rock are obtained by averaging the properties of the equilibrium mineralogies of the two end-member lithologies. Table 11.1 summarizes the basalt and harzburgite compositions in the NCFMAS system, comprising oxides of the elements Na₂O, CaO, FeO, MgO, Al₂O₃, and SiO₂. This chemical model accounts for ~98% of the mass of Earth’s mantle (e.g., Irifune [1994]).

The advantage of using basalt fraction as compositional variable is its simplicity relative to more complicated parameterizations and, not least, its relation to the dynamical processes that are responsible for generating and maintaining heterogeneities in the mantle as discussed earlier. Note, however, that if the real Earth is not well mixed chemically, it would very likely differ from the model invoked presently, calling for more complex scenarios. In the following, we concentrate on the MM model.

11.2.1.2. Phase Equilibrium Computations and Bulk Physical Properties

Our goal is to estimate density and elastic properties of minerals as a function of pressure, temperature, and composition. For this, two elements are required: (I) calculation of the stable mineral phases, their proportions, and their properties at the conditions of interest and (II) determination of bulk rock properties from single mineral properties. The determination of stable mineral phases as a function of pressure and temperature translates into a search for the amounts and compositions of mineral phases that minimize Gibbs free energy (a nonlinear function of composition), with the additional constraint of mass conservation. The input is represented by a number of chemical components that characterize a particular system in addition to pressure and temperature. The availability of comprehensive thermodynamic data sets for minerals and chemical compounds permits the computation of the geophysical properties of interest for the stable minerals. The computation of phase equilibrium is cast as an optimization problem, where the equations that need to be solved are of the form [Connolly, 2005]

$$G^{\text{sys}} = \sum_i^N \alpha_i G_i \quad \text{with} \quad \alpha_i \geq 0, \quad (11.3)$$

where G^{sys} is the Gibbs free energy of the system, G_i the Gibbs free energy of a certain amount (e.g., a mole) of the i th phase, and α_i the amount of the i th phase. A mass balance constraint is also taken into account, since the sum of the amount of the components within the phases must equal the corresponding amount in the system. Combination of thermodynamic data measured experimentally and the solution to the above minimization problem allows us to calculate which phases are stable at given conditions and their properties of interest. All free energy minimization computations were done using the *Perple_X* software package [Connolly, 2005] (www.perplex.ethz.ch).

Once stable mineralogy is obtained from Gibbs free energy minimization, physical properties (density and elasticity) of single minerals are determined by equation-of-state modeling, whereas properties of the aggregate are computed using averaging schemes that derive from composites theory (e.g., see Hill [1952], Watt *et al.* [1976], Guéguen and Victor [1994], and Berryman [1995]). A commonly employed scheme is the Voigt–Reuss–Hill (VRH) average [Hills 1952], which is constructed as the arithmetic mean from the Voigt (V) and the Reuss (R) bounds (corresponding to upper and lower bounds), respectively:

$$X_V = \sum_{i=1}^N f_i p_i, \quad X_R = \left(\sum_{i=1}^N \frac{f_i}{p_i} \right)^{-1}, \quad (11.4)$$

$$X_{\text{VRH}} = \frac{X_V + X_R}{2}, \quad (11.5)$$

where p_i and f_i are property and volume fraction of the i th mineral, respectively. Other averaging schemes exist—for example, Hashin–Shtrikman bounds [Hashin and Shtrikman, 1963], which are narrower than the Voigt and Reuss bounds—but entail making additional assumptions (e.g., Watt *et al.* [1976] and Berryman [1995]). Although not rigorously justified as a best estimate of the actual effective moduli [Stixrude and Jeanloz, 2007], we nonetheless follow common practice in the field (e.g., see Connolly and Kerrick, [2002], Connolly [2009], and Stixrude and Lithgow-Bertelloni [2005b, 2011]) and consider the VRH average as an estimator. For further discussion, the interested reader is referred, for example, to Berryman [1995], Stixrude and Jeanloz [2007], and Jones *et al.* [2009]. Here we compute only isotropic seismic wave speeds; however, anisotropic schemes have been developed [Stixrude and Lithgow-Bertelloni, 2011] but still lack a sufficient support from mineral physics data. To compute pressure at a point inside the Earth, we integrate the load from the surface. Finally, implicit assumptions of the Gibbs free energy minimisation approach include isotropy of the mineral aggregate, homogeneity of bulk composition, absence of elastic wave dispersion, and subsolidus conditions (no partial melt).

As an illustration of the thermodynamic approach, we computed phase equilibria and shear wave speeds (Figure 11.2) for the two end-member compositions discussed in Section 11.2.1.1 (Table 11.1) along the adiabat of Brown and Shankland [1981]. We observe clear differences in (1) stable mineralogy and computed S-wave speed profiles between the end-member models and (2) location and size of seismic discontinuities: olivine→wadsleyite (410 km) and ringwoodite→bridgemanite+ferropericlasite (660 km) vary considerably and depend strongly on the particular mineralogy and thus thermochemical setting. As shown and discussed in more detail in the next section, variations in physical properties strongly influence the seismic response, which, as a consequence, can be used to distinguish the various profiles and by inference the thermochemical state of the mantle.

The present thermodynamic model has limitations that may have consequences for its validity to Earth's mantle. First, the NCFMAS model system precludes consideration of redox effects that might be expected to be important if native or ferric iron is present in the Earth's mantle. We neglect such effects both out of necessity, in that the thermodynamic data required to model redox is

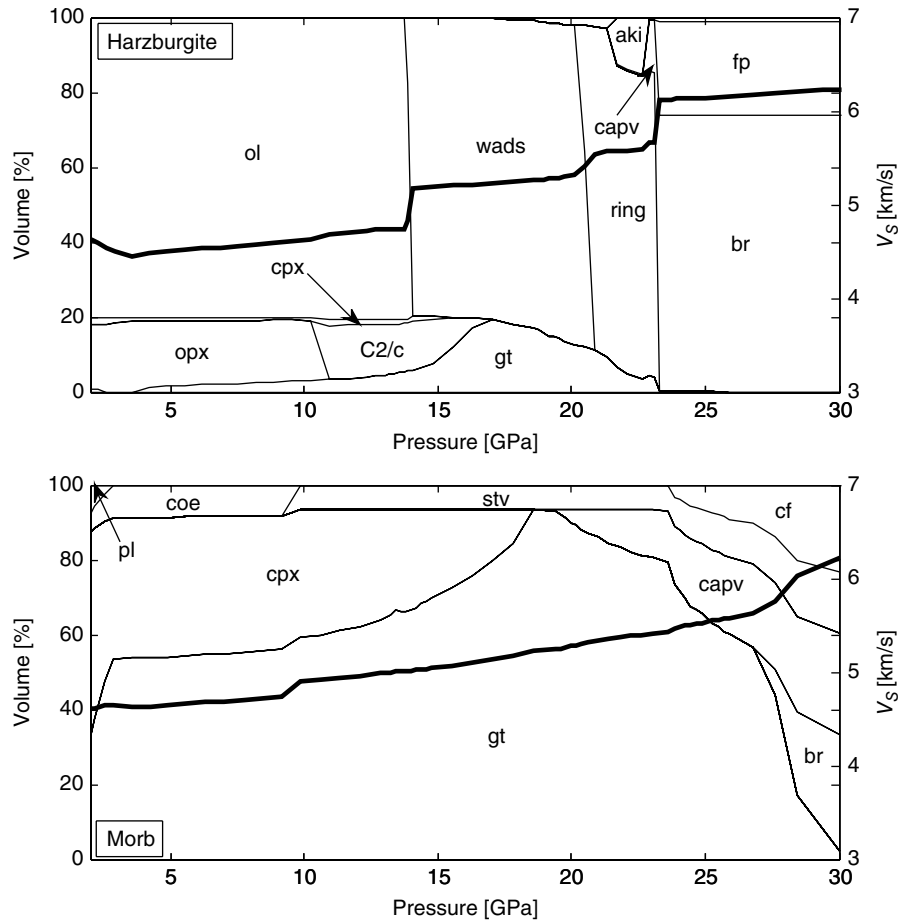


Figure 11.2 Variations in phase proportions (modal mineralogy) and seismic shear-wave speed (V_s) in the upper mantle, transition zone, and uppermost lower mantle (pressure range 2–30 GPa corresponding to 50 to 750 km depth). Isotropic shear-wave speed (*bold solid lines*) and phase equilibria are calculated for two different mantle compositions in the NCFMAS system (comprising oxides of the elements Na_2O , CaO , FeO , MgO , Al_2O_3 , SiO_2): harzburgite and morb, along the mantle adiabat of Brown and Shankland (1981) (not shown). Phases are: olivine (ol), orthopyroxene (opx), clinopyroxene (cpx), pl (plagioclase), coe (coesite), stv (stishovite), high-pressure Mg-rich cpx (C2/c), garnet (gt), wadsleyite (wad), ringwoodite (ring), akimotoite (aki), calcium silicate perovskite (ca-pv), ferropericase (fp), bridgemanite (br; formerly perovskite), and calcium ferrite (cf).

lacking, and simplicity, in that we are unaware of any work that suggests that ferrous iron is not the dominant form of iron in Earth's mantle. Components and phases not considered include H_2O , TiO_2 , Cr_2O_3 , and partial melt because of lack of thermodynamic data. Uncertainties associated with thermodynamic modeling are difficult to assess on account of the nonlinearity of the free-energy minimization problem and correlations among thermodynamic parameters—for example, bulk modulus and its pressure derivative. We conducted a Monte Carlo analysis of this uncertainty by considering the variance in a single parameter successively—that is, independent of the other parameters. The results indicate uncertainties in density and isotropic P- and S-wave speeds on the order of $\sim 0.1\%$, $\sim 0.5\text{--}1\%$, and $\sim 1\text{--}3\%$, respectively (unpub-

lished data). This particular type of statistical assessment tends to underestimate the overall uncertainty (cf. *Connolly and Kerrick* [2002], who estimate an uncertainty in seismic velocities of $\sim 1\text{--}3\%$ based on thermodynamic data). However, absence of the covariance between the various thermodynamic parameters leaves little alternative for now. Based on a different thermodynamic database than the one employed presently, *Kuskov et al.* [2014], in a study of the thermochemical structure of the lithospheric mantle beneath the Siberian craton find that the temperature at the lithosphere–asthenosphere boundary (LAB) are only accurate to within to $\pm 100^\circ\text{C}$. An alternative method for investigating this uncertainty is found in the study of *Afonso et al.* [2013a], who consider the problem of determining thermochemical structure of

the lithospheric mantle using a diverse set of geophysical data. Afonso and co-workers assess the uncertainty by comparing predicted and observed modal compositions for a set of xenoliths and generally find that differences between computed and observed values are within experimental error. Differences in physical properties between computed and laboratory measurements are also deemed negligible.

11.2.1.3. *Precomputed Tables: An Efficient Tool for Computing Properties*

The phase equilibria calculations hold a large part of the algorithm. This can be prohibitive, in particular in the framework of an inverse algorithm where typically many thousands of such calculations are required. The free energy minimization can be carried out in two ways: by static or by dynamic implementation. Static implementation means that given composition of rocks, we construct tables representing the requested properties (e.g., P- and S-wave speed, density) on the pressure-temperature space. In this way it is possible to precalculate the seismic properties of the mantle for several given compositions as a function of pressure and temperature and store these in multidimensional tables as done in *Zunino et al.* [2011]. Any property can then be obtained by simple table look-up and interpolation. The other approach is the dynamical implementation: Given a particular value for pressure, temperature, and composition, we compute the resulting properties minimizing Gibbs free energy during the inversion process. Here we will focus on the static implementation (called *Phemgp*) and construct tables of properties for the two end-member compositions listed in Table 11.1.

With this technique, computation of bulk rock properties, such as density and seismic velocities, becomes very fast and reliable. Once the tables are computed, only interpolation is involved. The only caveat is that the range of variation in pressure, temperature and compositional parameters need to be anticipated in advance in order to construct the look-up tables. In principle, this could have a significant impact on memory requirement depending on the resolution needed, since, for the sake of speed, tables have to be kept in memory during the process; however, we verified that at the resolution necessary for our applications, the amount of memory used is well within the standard capacity found on a modern personal computer. Precomputed look-up tables for the two end-member composition considered here and programs to extract properties from these are available from <http://www.perplex.ethz.ch/phemgp/phemgp.html>.

11.2.1.4. *Effects of Compositional and Thermal Variations on Elastic Properties*

Examples of mantle properties obtained by *Phemgp* for basalt and harzburgite—that is, for basalt fractions of 0 and 1, respectively—are shown in Figure 11.3 and

illustrate the influence of phase equilibria on mantle seismic and density structure. Properties extracted with *Phemgp* along representative mantle geotherms reveal prominent features associated with the major mineral phase transformations and the major seismic discontinuities at 410-, 520-, and 660-km depth. These transitions, which cause strong seismic velocity gradients, clearly depend on temperature, pressure, and composition.

To further illustrate the effect of temperature and compositional variations on mantle properties, we calculated properties as resulting from perturbations applied to a reference state. As reference geotherm we rely on the continental geotherm of *Turcotte and Schubert* [2002] and as reference composition we employ a basalt fraction of 0.2. Reference continental and modified geotherms are shown in Figure 11.4.

Properties extracted from the tables along the various geotherms and compositions and mixed according to Eq. (11.2) are summarized in Figure 11.5. Perturbations on the major phase transitions, particularly olivine → wadsleyite and wadsleyite → ringwoodite, are strongly influenced by temperature variations. Both the “410” and the “520” move deeper as temperature increases, in line with theoretical considerations [*Bina and Helffrich*, 1994] and observations [*Helffrich*, 2000]. The “660” appears to be less influenced. Changes in properties with temperature (i.e., size of discontinuity) across the transitions are almost negligible. Variations in properties due to compositional changes, on the other hand, are clearly more complicated and include relatively strong perturbations in all seismic discontinuities in both location and size. For a basalt fraction of 1, for example, the “410” is entirely absent, while the “660” moves well below 700 km depth (cf. Figure 11.5).

These observations have also been discussed in a recent seismic tomography study where surface-wave dispersion data across the Australian continent were inverted for mantle thermochemical structure using the same methodology proposed here and the parameterization shown in Figure 11.6 [*Khan et al.*, 2013] (to be discussed further in Section 11.3). Analyzing transition zone topography—that is, variations in depth to the major discontinuities in and around the transition zone (Figure 11.7)—*Khan* and co-workers found that the “410” correlated strongly with temperature, while the behavior of the “520” was somewhat diminished relative to the “410”. The “660”, on the other hand, was clearly found to correlate negatively with temperature. Variations with composition were, as indicated above, more complicated with the “660” correlating positively with Fe# ($\text{Fe}/(\text{Fe} + \text{Mg})$) and “410” and “520” showing negative correlation, while all three discontinuities were observed to correlate positively with $(\text{Mg} + \text{Fe})/\text{Si}$ (these features are discussed in more detail in *Khan et al.* [2009]). Although surface waves are not ideal for imaging seismic discontinuities, the important point to

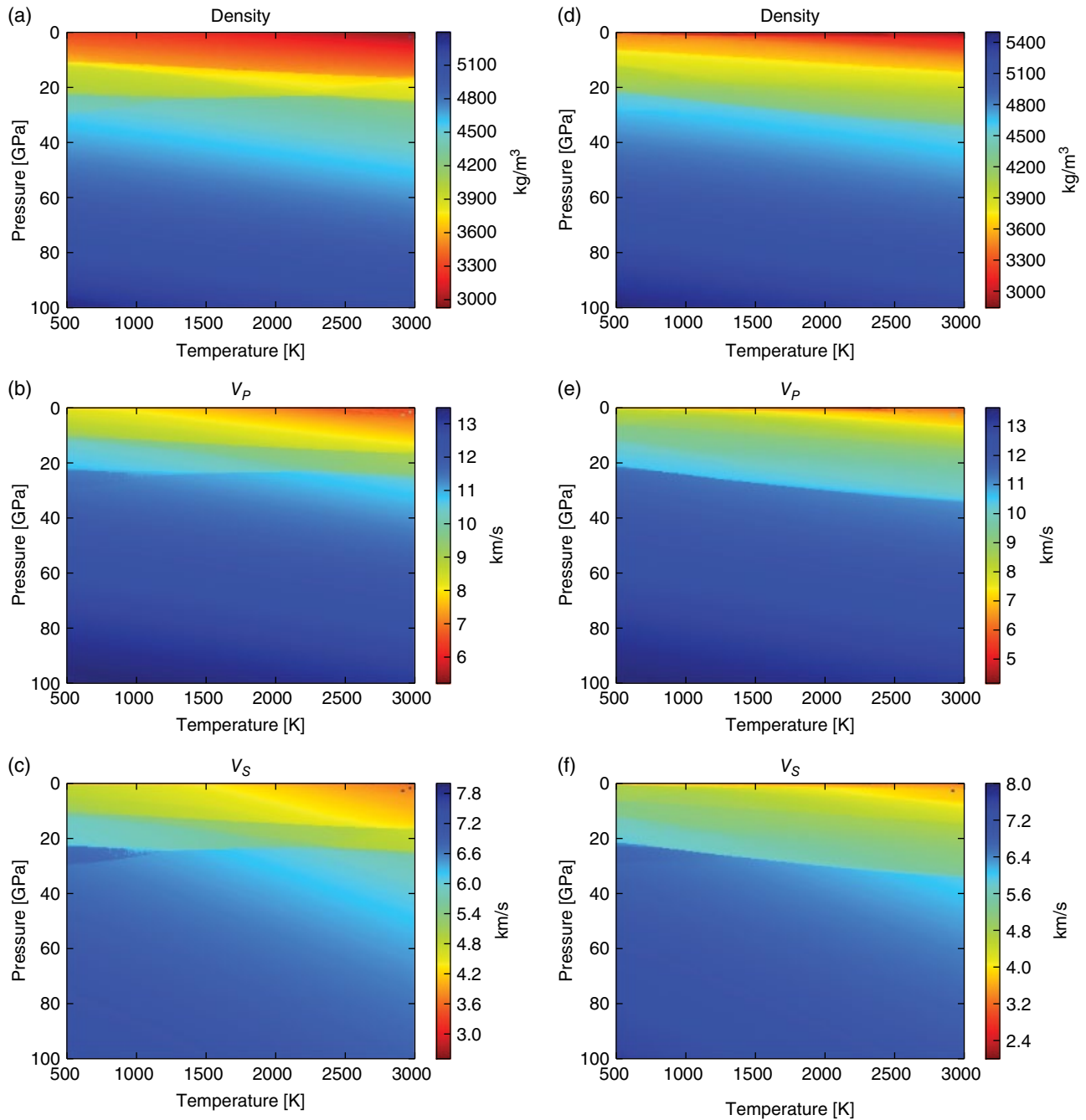


Figure 11.3 Density and isotropic P- and S-wave speeds (V_P and V_S) of the mantle computed for harzburgite (plots **a–c**) and basalt (plots **d–f**) compositions (see Table 11.1).

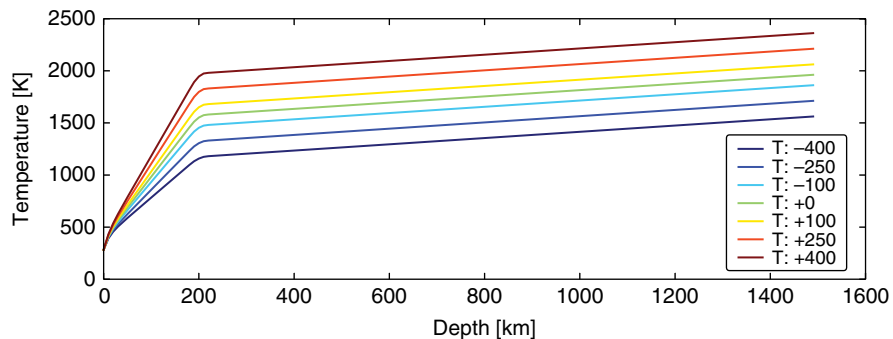


Figure 11.4 Continental reference and modified geotherms. “T” indicates relative temperature perturbation (in K) with respect to the reference continental geotherm of *Turcotte and Schubert* [2002] ($T:+0$). See main text for details.

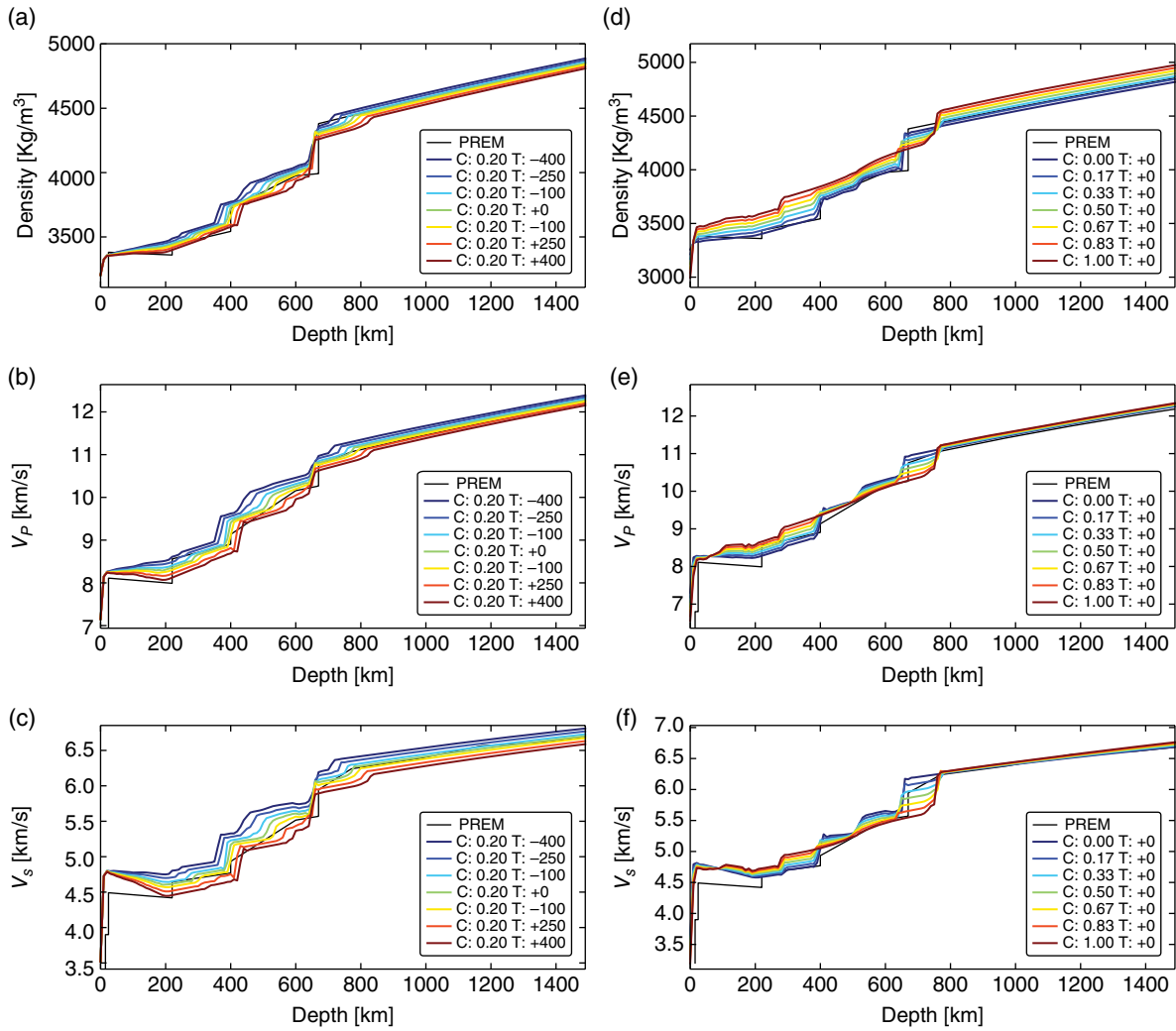


Figure 11.5 Profiles of density and isotropic seismic wave speeds V_p and V_s as a function of depth for the geotherms (a-c) shown in Figure 11.4 and various basalt fractions (d-f). “T” indicates relative temperature perturbation with respect to reference geotherm (T:+0) and “C” variation in basalt fraction. PREM profile is shown in black.

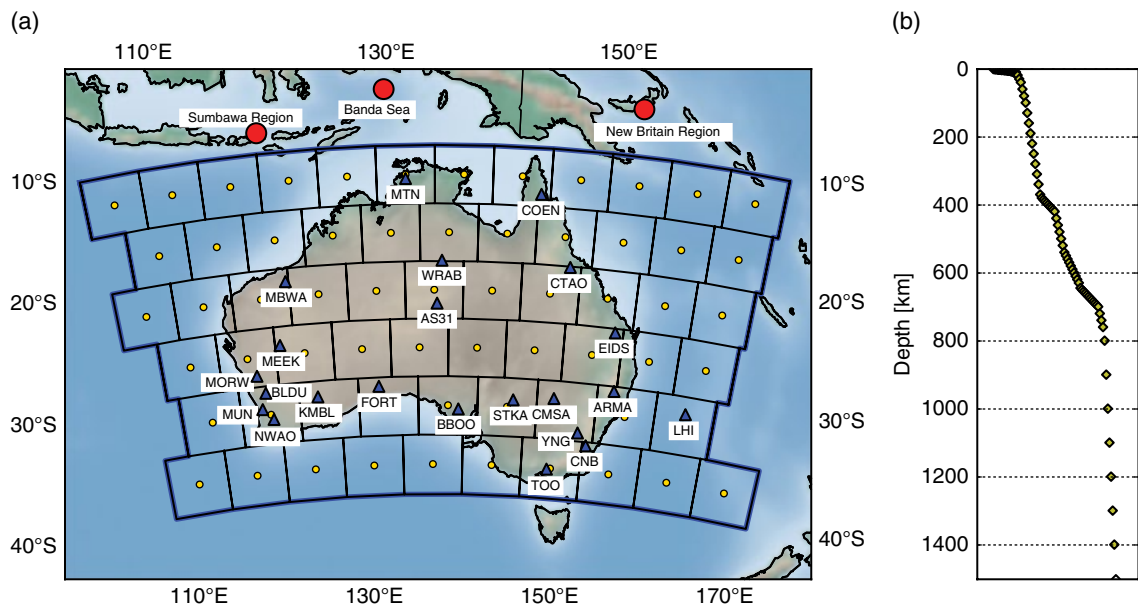


Figure 11.6 Lateral (a) and vertical (b) parameterization of the area used in the surface-wave-based tomography study. Yellow circles represent the centers of “pixels” (a), and yellow diamonds represent depths of nodes (b). Blue triangles indicate seismic stations, and red circles indicate earthquake epicenters. See main text for details.

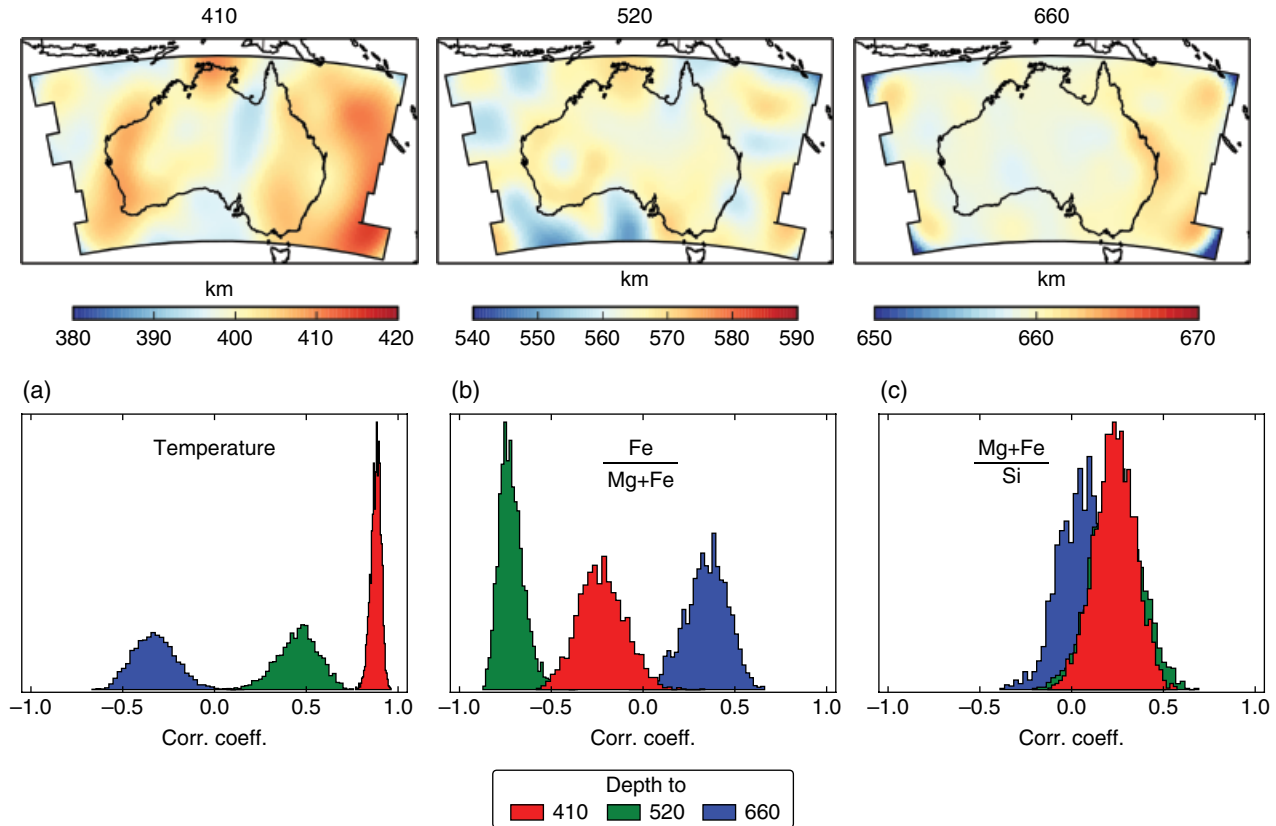


Figure 11.7 Mean depths to “410”-, “520”-, and “660”-km seismic discontinuities beneath continental Australia marking the transition between upper mantle and transition zone, the mid-transition zone discontinuity, and the transition to the lower mantle as defined by the mineral phase transformations: olivine→wadsleyite, wadsleyite→ringwoodite, and ringwoodite→ferriperovskite+bridgmanite, respectively (see Figure 11.2 for location and notation of mineral phases). The images were computed from an ensemble of $\sim 10^4$ models obtained from stochastic inversion (see *Khan et al.* [2013] for details) and represent the statistical mean of these models. Plots a–c show correlation between transition zone depth and thermochemical parameters (composition is shown as variations of $\text{Fe}/(\text{Fe} + \text{Mg})$ and $(\text{Mg} + \text{Fe})/\text{Si}$). Distributions are normalized to unity for the highest peak in each plot and are independent between the various properties shown.

note is that much of the structure visible in the images at the base of the upper mantle, for example, derives from lateral variations in phase transitions associated with the olivine→wadsleyite transformation. The corresponding lateral variations in velocity were observed to be much larger than those associated with purely lateral variations in temperature and composition immediately above and below the transition (see also *Stixrude and Lithgow-Bertelloni* [2007]). Neglect of this contribution to lateral structure very likely results in lateral variations in temperature, or structure in general, that vary too rapidly and probably also too strongly as apparent in some studies (e.g., see *Goes et al.* [2005] and *Trampert et al.* [2004]). Extension of the methodology to include seismic data sensitive to discontinuities and transition-zone structure such as PP and SS precursors and receiver functions (e.g., see *Schmerr and Garnero* [2006], *Tauzin et al.* [2008, 2013],

Shmandt et al. [2014], *Schmerr* [2015], and *Thompson et al.* [2015]) will be considered in the future.

11.2.2. Seismic Wavefield Modeling

The availability of modern broadband catalogs of seismic data, together with improved numerical modeling of seismic waveforms, has opened up the opportunity to explore Earth’s interior more accurately and in more detail than previously possible (e.g., see *Komatitsch et al.* [2002], *Fichtner et al.* [2009], and *Cupillard et al.* [2012]). The possibility to invert entire waveforms has opened a new chapter in seismic tomography. Dealing with waveforms means exploiting all the information contained in seismograms, which in principle leads to a significant improvement in the amount of information we can extract from the subsurface.

11.2.2.1. Seismological Tools

The seismic data used to image the Earth's interior range from body-wave travel times and surface-wave dispersion curves to entire waveforms that include both phase and amplitude information. Correspondingly, the methods used to compute synthetic data can be divided in a few major classes: ray-based, normal-mode summation, direct solvers, finite differences and spectral-element methods [Liu and Gu, (2012)]. Ray-based methods rely on the assumption of infinite frequency, which collapses the sensitivity to a ray and allows travel times to be computed by solving the eikonal equation. These methods are computationally very fast, but become inappropriate when the size of heterogeneities in the Earth's model is close to the wavelength of the seismic wavefield. The normal-mode-based approach instead is capable of very accurate calculations, but the computational load increases very quickly with the order, making this approach intractable for probabilistic tomography.

Thanks to theoretical advances, a novel technique termed finite-frequency tomography [Dahlen *et al.*, 2000] has gained popularity among seismologists. This technique takes into account the frequency dependence of the sensitivity of seismic waves. It is used to compute finite-frequency sensitivity kernels, which can be employed for solving the inverse problem. These kernels are characterized by a sensitivity which spans a certain volume around the ray path, such that substantial portions of the model have influence on the seismic response at the surface (e.g., see Montelli *et al.* [2004]).

Eventually, the method that has emerged as the best compromise between accuracy and computational cost is the Spectral Element Method (SEM) (e.g., Komatitsch and Vilotte [1998]). It is able to solve the wave equation to very high precision, as it provides an exponential decrease of the aliasing error with the increase in the order of the polynomial basis functions. This numerical property is the so-called spectral precision, from which the name SEM derives.

The elastic wave equation describing the displacement \mathbf{u} can be written as

$$\rho \frac{\partial^2 \mathbf{u}}{\partial t^2} = \nabla \cdot \mathbf{T} + \mathbf{f}, \quad (11.6)$$

where ρ is the density, t the time, \mathbf{T} the stress tensor, and \mathbf{f} the body force. This equation together with the linear constitutive stress-strain relation (Hooke's law)

$$\mathbf{T} = \mathbf{C} : \boldsymbol{\varepsilon}, \quad (11.7)$$

where \mathbf{C} is the fourth-order stiffness tensor and $\boldsymbol{\varepsilon}$ the strain tensor ($\boldsymbol{\varepsilon} = \frac{1}{2}(\nabla \mathbf{u} + (\nabla \mathbf{u})^t)$), forms the elastodynamic problem. Usually, at the surface of the Earth, a

homogeneous Neumann boundary condition is imposed ($\hat{\mathbf{n}} \cdot \mathbf{T} = \mathbf{0}$, where $\hat{\mathbf{n}}$ is the normal to the surface), but other conditions can be used, such as absorbing boundaries at the edges of the domain in the case of regional-scale studies. The SEM solves the elastodynamic problem in the weak form and yields the full seismic wavefield, including all seismic phases. The spatial domain of the model is decomposed into hexahedral elements, and high-order Lagrange polynomials defined on Gauss-Lobatto-Legendre (GLL) points are employed for the functional discretization. These polynomials, in addition to a GLL quadrature for evaluating the integrals, make the mass matrix diagonal, which significantly reduces the computational cost. One ends up with a discretized linear ordinary differential equation in time:

$$\mathbf{M}\ddot{\mathbf{U}}(t) + \mathbf{K}\mathbf{U}(t) = \mathbf{F}(t), \quad (11.8)$$

where \mathbf{M} is the mass matrix, \mathbf{K} the stiffness matrix, and $\mathbf{F}(t)$ the source term. Solving Eq. (11.8), with the use of a classic finite-difference scheme in time, yields the entire seismic wavefield for a given source term. The latter is usually in the form of a source time function and a moment tensor that can be retrieved from available earthquake catalogs such as the centroid moment tensor (CMT) catalog [Dziewonski *et al.*, 1981; Ekström *et al.* 2012]. Note that CMT solutions are the result of an inverse problem that relies on waveform data. In principle, therefore, when modifying the seismic velocity model, changes in the moment tensor should also be taken into account. However, the trade-off between source mechanism and Earth structure is beyond the scope of this paper. For simplicity, we assume the CMT solution retrieved from the CMT catalog to be the correct source mechanism.

In this work we rely on RegSEM [Cupillard *et al.*, 2012], an implementation of the SEM for regional-scale simulations. The workflow consists of two main processes: (1) meshing (i.e., defining the three-dimensional grid where the wavefield will be propagated) and (2) solving the wave equation on the mesh. RegSEM uses hexahedral meshes where the size of the elements depends on the minimum wavelength that has to be propagated. Thus, the higher the frequency to be simulated, the higher the computational cost. This becomes prohibitive for Monte Carlo-like methods, where many forward iterations are required. This is the main reason why, at present, we have to limit our study to long-period seismic data (see Section 11.2.2.2).

11.2.2.2. Parameterization, Meshing, Homogenization

To simulate the propagation of seismic waves through the Earth, we have to define a parameterization of our model of elastic properties which accommodates the

structures we are interested in and follows the requirements of the chosen strategy for forward modeling. Generally, parameterizations can be divided in two categories: relying on global bases such as spherical harmonics or local bases in the form of cell, node or spline-based grids. The choice of the parameterization has to be adapted to the forward solver and the specific problem under study, as no single approach can be considered universally superior to all others.

The first step to perform seismic forward modeling with the SEM is to define a mesh upon which density and P- and S-wave velocities (and possibly additional parameters such as anisotropic parameters) are assigned. The values of those properties are obtained from the thermodynamic calculations described above. Typically, seismic solvers for the SEM require to pick values of the needed parameters at several points (GLL points) within each mesh element, in a possibly nonsimple spatial arrangement, so, practically speaking, it is required to be able to provide values of properties at any given point in the domain and because of this some form of interpolation is needed.

Meshing the Earth can be a very complex task because of the spherical shape and the various discontinuities and inhomogeneities that should be accommodated. For the spectral element method, structured hexaedral meshes are generally used, which discretize the wave equation and use a functional representation on these grids. The choice of the grid spacing is not arbitrary, but must satisfy some conditions to ensure proper convergence of the solution and thus adapt to the characteristics of the wavefield to be propagated. This translates in a set of rules to constrain the maximum grid spacing allowed for propagating a certain maximum frequency of the wavefield and the time stepping of the algorithm. For instance, for RegSEM, two conditions must be satisfied [Cupillard *et al.*, 2012],

$$d \geq \frac{N}{5} \lambda_{\min} \quad \text{and} \quad \Delta t \leq C \left[\frac{\Delta x}{V_p} \right]_{\min}, \quad (11.9)$$

where d is the size of the elements in the mesh, N is the polynomial order, λ_{\min} the minimum wavelength, Δt the time step, C the Courant number (usually chosen between 0.3 and 0.4), Δx the grid spacing, and V_p the P-wave speed. The first condition dictates the maximum size of the elements of the mesh allowed to propagate a wavefield with a minimum wavelength of λ_{\min} and is empirically derived. The second condition, the Courant–Friedrichs–Lewy (CFL) condition, ensures stability of the time-marching by setting the time step Δt . These conditions have a strong impact on the computational burden because the smaller the size of the elements of the mesh and the time step, the greater the amount of time it takes to compute the solution.

It can be shown that the band-limited nature of the observed seismic data has the consequence that the heterogeneities whose size is smaller than the minimum wavelength only affect the wavefield in an effective way; in other words, what can be “seen” from the point of view of the observations is an upscaled version of the medium (e.g., see Backus [1962] and Capdeville *et al.* [2013]). Theoretical and technical advances [Capdeville *et al.*, 2010a,b; Guillot *et al.*, 2010; Capdeville *et al.*, 2015; Cupillard *et al.*, 2015], permit us to calculate such upscaled medium in terms of elastic parameters provided the shortest wavelength traveling in the medium. The resulting homogenized model, being a smoothed version of the original, can be used to alleviate the computational burden deriving from performing complex and high-resolution meshing in the presence of sharp discontinuities and small heterogeneities. Further, in the case of models parameterized in terms of large blocks, as could be the case for long-period data, it may help decreasing the computation time by allowing coarser meshes to be used.

11.2.2.3. Effects of Thermal and Compositional Variations on Seismic Data

As shown in Section 11.2.1, temperature and composition are observed to strongly impact Earth’s elastic properties. To assess the effects of such variations on the seismic response of the Earth, we performed numerical simulations where we computed full waveforms using the models shown in Figure 11.5. For illustration, we calculated the seismic response at station STKA (Stephens Creek, SA, Australia) (see Figure 11.6) for a 6.5-magnitude earthquake that occurred on November 25, 2007 in Indonesia. For the purpose of computing seismograms based on one-dimensional models, we employed the waveform code AxiSEM [Nissen-Meyer *et al.*, 2014], where attenuation was taken into account by interpolating PREM [Dziewonski and Anderson, 1981] values. Figure 11.8 shows the resulting vertical-component seismograms for the various models, which were computed down to 10-s period. Temperature-induced variations of the calculated ground displacement appear relatively smooth and are mostly characterized by phase shifts and only a modest impact on amplitude. In contrast, composition has a more pronounced influence, changing both amplitude and phase, which reflects the more complex variation in physical properties incurred by compositional changes (cf. Figure 11.5).

11.3. POSTERIOR FILTERING OF TOMOGRAPHIC MODELS—THE AUSTRALIAN SUBCONTINENTAL MANTLE REVISITED

In this section, we illustrate how actual thermochemical models of the mantle (beneath continental Australia) obtained from inversion of surface-wave dispersion data

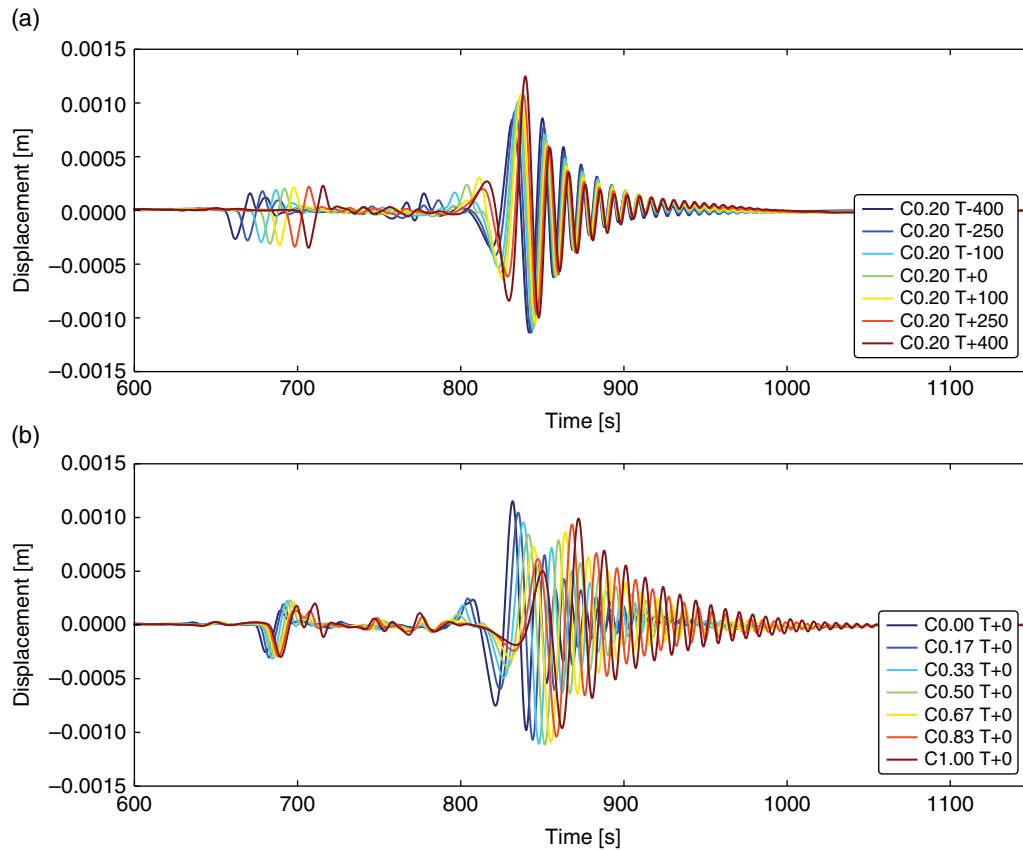


Figure 11.8 Seismograms computed from the radial profiles shown in Figure 11.5 down to 10-s period as recorded on the vertical component at station STKA (see Figure 11.6) at a distance of about 3500 km. The source is a magnitude-6.5 earthquake that occurred on November 25, 2007 in Indonesia. “T” indicates the relative temperature perturbation in Kelvin with respect to the reference geotherm ($T + 0$), while “C” refers to basalt fraction.

can be further refined by using additional data (waveforms). For completeness, we first briefly summarize the approach used in inverting surface-wave phase-velocity dispersion curves and describe the results (for details the reader is referred to *Khan et al.* [2013]), after which follows computation of waveform data using the surface-wave based tomographic models and comparison to observations.

11.3.1. Inversion of Surface-Wave Phase Velocity Dispersion Curves

The measured data consist of the azimuthally averaged isotropic part of the global azimuthally anisotropic phase-velocity maps of fundamental and higher-mode Love (to fifth overtone) and Rayleigh (to sixth overtone) waves of *Visser et al.* [2008]. Overtones have enhanced sensitivity in depth relative to fundamental-mode data and thus help to constrain regions below the upper mantle. The model was parameterized laterally (longitude and latitude) as an unstructured grid of “pixels” each spanning an area of about 5×5 degrees, whereas in depth a series of non-evenly spaced nodes was used. Figure 11.6a shows the grid of “pixels” along with the

pixels’ centers where phase-velocity dispersion curves were extracted from the phase-velocity maps of *Visser et al.* [2008]. The depth parameterization consists of a series of non-evenly spaced nodes where parameters (e.g., crustal structure, Moho depth, composition, temperature, anisotropy, and anelasticity) are defined. Values for all these parameters are interpolated to the depth nodes shown in Figure 11.6b. To take into account crustal effects, we use CRUST2.0 [*Bassin et al.*, 2000] as initial model and apply perturbations laterally to both structure and Moho depth.

The prediction of Rayleigh- and Love-wave dispersion data from thermochemical parameters is shown in Figure 11.9, which summarizes the entire forward problem. The g_n ’s correspond to different physical theories and the various symbols to model and data parameters (see Table 11.2). Computation of anisotropic and anelastic parameters are described in Appendices B and C.

We employed a Markov chain Monte Carlo method to invert the data (see Appendix A). We considered Rayleigh- and Love-wave dispersion curves for each “pixel” independently and inverted these for radial models of the parameters that are summarized in Table 11.2.

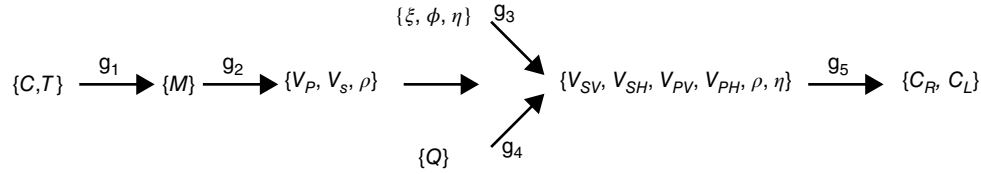


Figure 11.9 A schematic illustration of the forward problem and the different model parameters (c , T , ξ , ϕ , η), physical theories (g_1 , g_2 , ...), and data (C_R , C_L) used to describe it. Symbols are described in Table 11.2.

Table 11.2 Model and Data Parameters and Connections Between the Various Parameters (Physical Laws)^a

Model and Data Parameter	Description
C	Composition (primary)
T	Temperature (primary)
M	Mineralogy (secondary)
V_P, V_S, ρ	P- and S-wave speed, density (secondary)
ξ, ϕ, η	Anisotropic parameters (primary)
Q	Attenuation (primary)
$V_{PV}, V_{PH}, V_{SV}, V_{SH}$	Anisotropic anelastic parameters (secondary)
C_R, C_L	Rayleigh- and Love-wave dispersion data
Physical Laws	
g_1	Thermodynamic modeling
g_2	Equation-of-state modeling
g_3	Anisotropic correction
g_4	Anelastic correction
g_5	Prediction of surface-wave dispersion

^a Note that we only invert for primary parameters; secondary parameters depend on primary parameters (see *Khan et al.* [2007] for a detailed discussion).

11.3.2. The Posterior Movie

In comparison to deterministic inverse methods where the output is a single best-fit, typically smooth model, the probabilistic approach provides a whole ensemble of models that fit data within uncertainties (~ 5000 have been selected for analysis here). All of these models constitute the output, represented by the posterior distribution $\sigma_M(\mathbf{m})$ [see Equation (11.A1)]. The posterior distribution is usually a high-dimensional probability density function that is notoriously difficult to visualize in a plot. Depending on the characteristics of the posterior distribution (e.g., multimodality), central estimators such as the mean value, which are easy to plot, do not provide a meaningful representation of the actual models. As an alternative strategy to single estimators, *Tarantola* [2005] has advocated the construction of a “movie” by sequentially showing samples from the posterior distribution.

General features that are characteristic of the models, such as those that are well-resolved, will tend to be recurring in the posterior images, whereas less well-resolved features will appear much more scattered. Data-related structural patterns are easily separable from those that appear randomly and in a noncoherent and nonrecurring fashion. Although posterior models can differ significantly, they are nonetheless models with high likelihood values that predict observed data within uncertainties.

For present purposes, we created a movie showing several properties of the mantle using 250 randomly chosen models from the posterior. The movie is available online (www.nbi.dk/~zunino/publsm.html) as supplemental material and depicts the following properties between 100- and 800-km depth: S-wave velocity, density, temperature, compositional parameters [(Mg + Fe)/Si and Fe/(Mg + Fe)], and mineralogy [px/(ol + px) and fp/(br + fp)]. A single model from the posterior distribution is shown in Figure 11.10.

Strong correlation between shear-wave speed and density anomalies is observed in the upper mantle, which also outlines the continental boundaries of the region. The continental regions appear to have a distinct thermochemical signature and are divided into slow [corresponding to “hot” with relatively low (Mg + Fe)/Si and high Fe/(Mg + Fe) values] and fast [corresponding to “cold” with relatively high (Mg + Fe)/Si and low Fe/(Mg + Fe) values] patterns that extend well into the upper mantle. Toward the bottom of the upper mantle, we observe that thermal effects are becoming progressively less important and give way to more complex structures that appear to be compositionally driven. This is most apparent in the case of density at 300-km depth, which reveals a relatively strong compositional signature that correlates positively with Fe/(Mg + Fe). The behavior of the shear-wave speed anomalies, in contrast, are mostly governed by thermal effects.

11.3.3. Comparison with Other Tomographic Models

The shear-wave speed variations found here in the upper mantle have also been reported elsewhere (e.g., see *Fichtner et al.* [2010] and *Fishwick and Rawlison* [2012]). These models are sensitive to about 200- to 250-km depth. The model of *Fichtner et al.* [2010] (hereafter FCT) was obtained using full waveform tomography, whereas

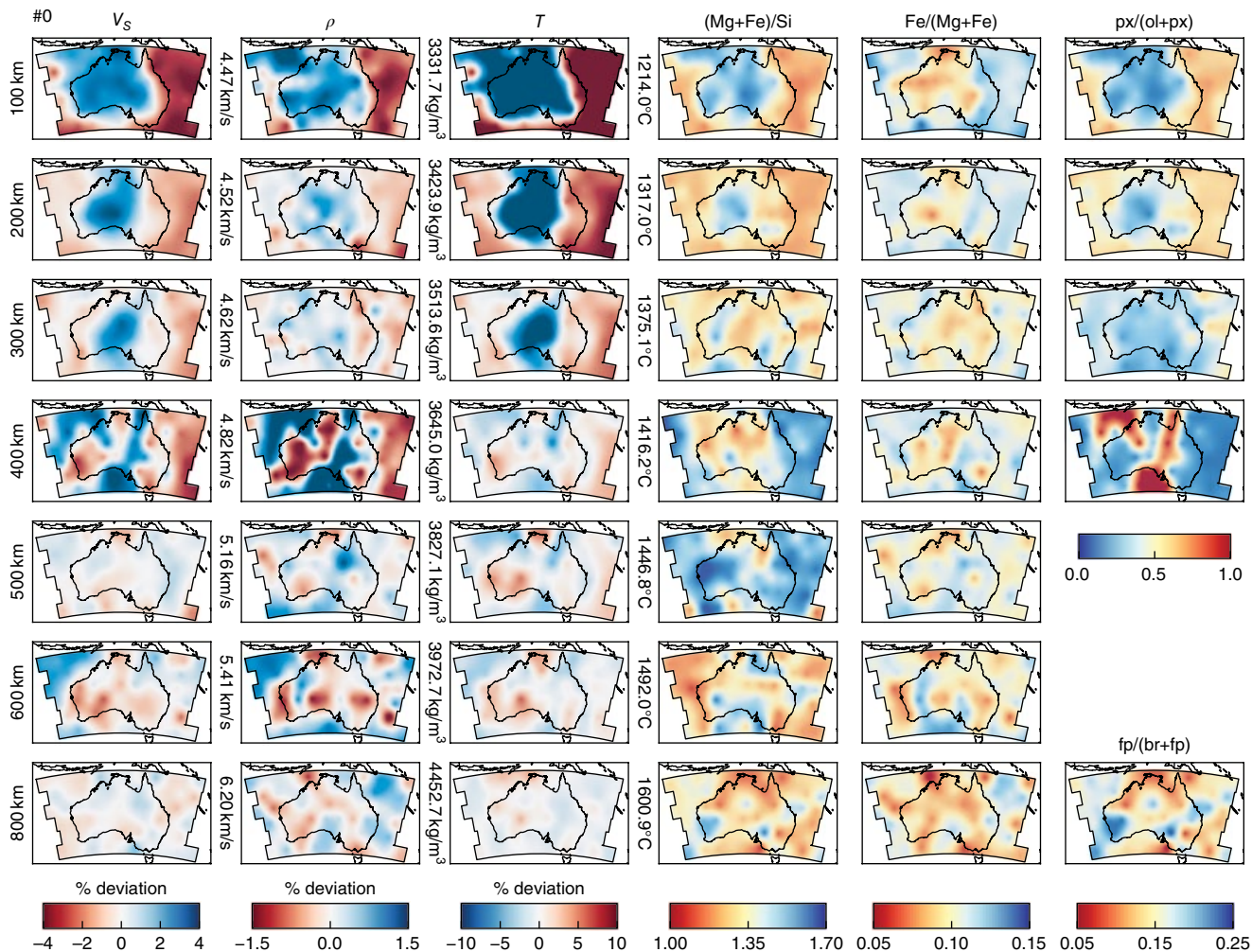


Figure 11.10 A model taken randomly from the posterior distribution showing shear-wave speed (V_s), density (ρ), temperature (T), compositional parameters [(Mg + Fe)/Si and Fe/(Mg + Fe)], and mineralogy [$\text{px}/(\text{ol} + \text{px})$ and $\text{fp}/(\text{br} + \text{fp})$]. For phase names see Figure 11.2. See main text for details.

Fishwick and Rawlinson [2012] (hereafter FSW) considered fundamental-mode surface-wave data. In Figure 11.11 the S-wave models of FCT and FSW are compared with our results using the 95% credible interval [Chen and Shao, 1998], the mean model, and the maximum likelihood model. These models are interpolated on a common grid by using radial basis functions. The lateral resolution of our models, compared to FCT and FSW, is lower, as is apparent from their smoothness. The most distinct features of these tomographic models include, much as observed here, separation of structure into slow and fast tectonic regimes.

To provide a more quantitative comparison of the models, we computed the correlation coefficient for each sampled posterior S-wave model and FCT and FSW, respectively, at depths of 100 km and 200 km. For this purpose, FCT and FSW were interpolated on the grid

shown in Figure 11.6 using radial basis functions. The resulting correlation coefficients are shown in Figure 11.12. At 100-km depth, the correlation between our models and FCT is ~ 0.79 , whereas for FSW the correlation increases to ~ 0.92 . At 200-km depth, the correlation coefficients are slightly lower than at 100-km depth, but remain relatively high, with coefficients of 0.76 (FCT) and 0.89 (FSW), respectively. Interpolation on alternative common grids with different resolution did not significantly change the distribution of correlation coefficients. Thus, and in spite of differing methodologies, data, and parameterizations, we find good agreement between our ensemble of models and the tomographic models FCT and FSW. The overall level of agreement with other regional models is encouraging and we consider this evidence in support of the joint thermodynamic analysis.

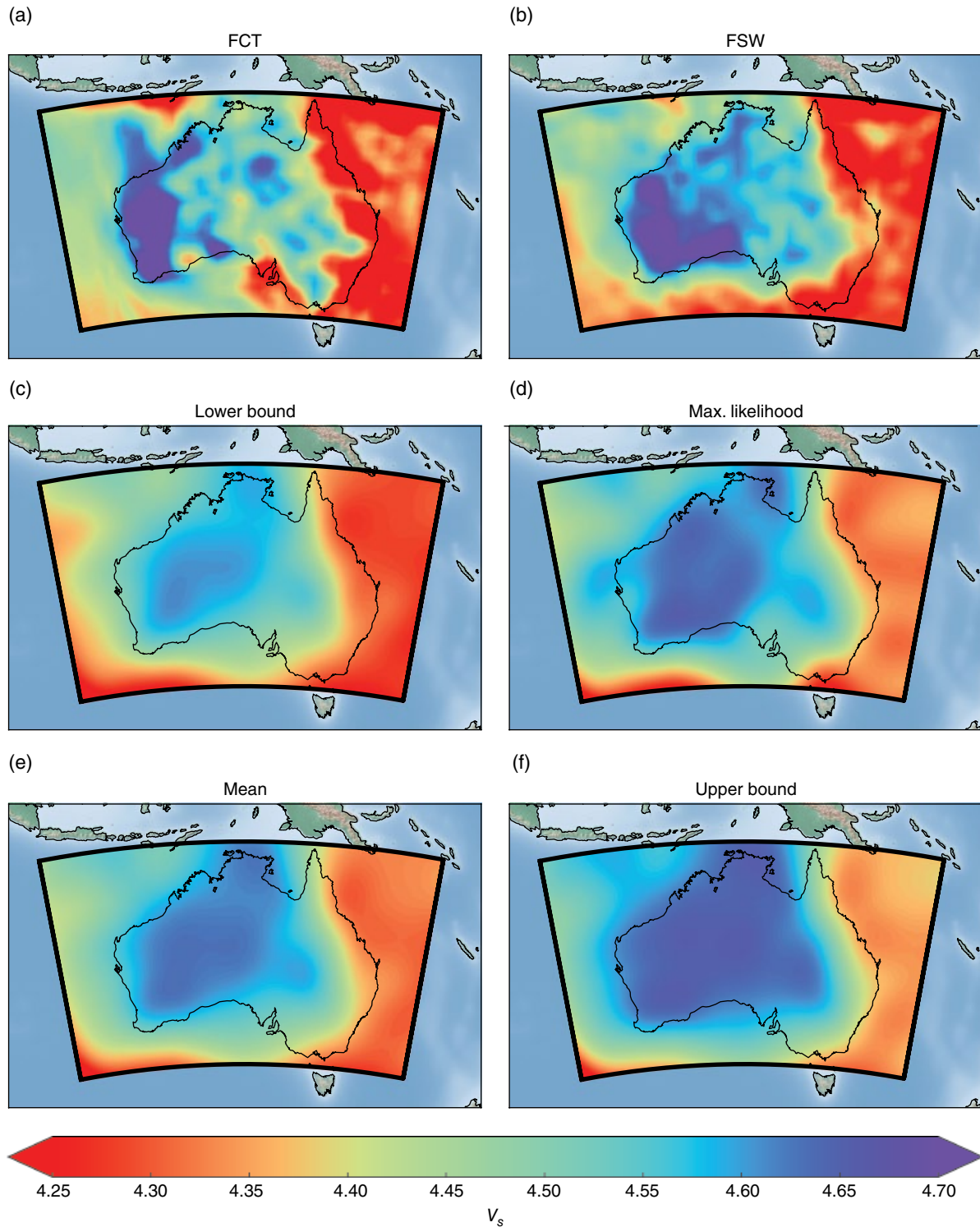


Figure 11.11 Comparison of regional tomographic models in the form of isotropic shear-wave models at 100-km depth from (a) *Fichtner et al.* [2010] (FCT), (b) *Fishwick and Rawlinson* [2012] (FSW), and models obtained from inversion of surface-wave dispersion data (*Khan et al.* [2013]) (c–f). Plots c and f indicate lower and upper credible intervals (95%), respectively, plot e indicates mean model, and plot d indicates the maximum likelihood model.

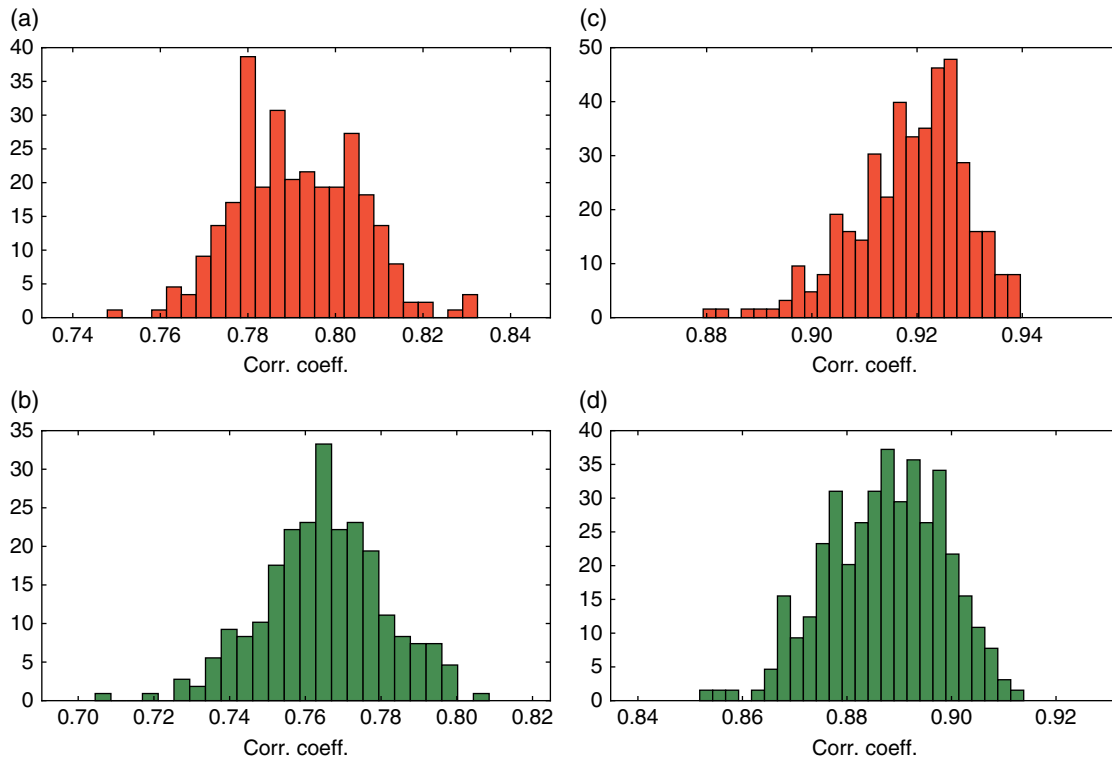


Figure 11.12 Computed correlation between surface-wave based models shown in plots c–f of Figure 11.11 and the regional tomography models of *Fichtner et al.* [2010] (**a,b**) and *Fishwick and Rawlinson* [2012] (**c,d**). First row shows correlation of models at 100 km of depth, and second row shows correlation at 200 km of depth. See main text for details.

11.3.4. Full Waveform Calculations

To further refine our collection of posterior models, we compute waveforms at 20-s period for a set of our surface-wave-based tomography models. We picked six models randomly from the posterior distribution and computed seismograms using RegSEM.

To reduce the computational costs of running RegSEM down to 20-s period and to prevent propagation of spurious reflections related to the relatively low-resolution input models, we utilized vertical homogenization, based on the concept of an “effective medium” (e.g., see *Capdeville et al.* [2013]) (cf. Section 11.2.2.2). As sources, we used three earthquakes that occurred north of Australia. These include the 6.4-, 6.5-, and 6.4-magnitude events in the regions of Sumbawa, New Britain, and the Banda Sea, respectively (see Figure 11.6). The moment tensor data were retrieved from the global CMT catalogue [*Dziewonski et al.*, 1981; *Ekström et al.*, 2012]. The models are meshed using a structured grid that spans an area of about 46 degrees in longitude and 48 degrees in latitude (centered around 136° W, 23° S). Additionally, perfectly matched layer (PML) boundary conditions were applied to the edges of our grid.

Computed and observed seismograms are shown in Figure 11.13. Observed data have been processed to remove instrument response by deconvolution and filtered according to the parameters used for the source-time function employed in our simulations (the source time spectrum is defined by four corner frequencies: 0.002, 0.005, 0.03, and 0.05 Hz). We generally observe that the phase of the computed seismograms is reasonably well fit for most stations, but that the amplitude is off, which is to be expected given the nature of the input models. Nevertheless, this comparison reveals that much is to be gained by this type of analysis. In particular, the inversion of seismic waveforms has proved to be a strong tool to image Earth’s interior, and wedding the methods proposed here with stochastic waveform inversion is an important next step. As shown by *Käuffl et al.* [2013], and in spite of the huge computational requirements, stochastic long-period waveform inversion is feasible. While this evidently limits us to large-scale structures only, stochastic waveform inversion provides a powerful means of rigorously assessing measures of uncertainty, accuracy, and resolution—properties of tomographic models that are currently not available.

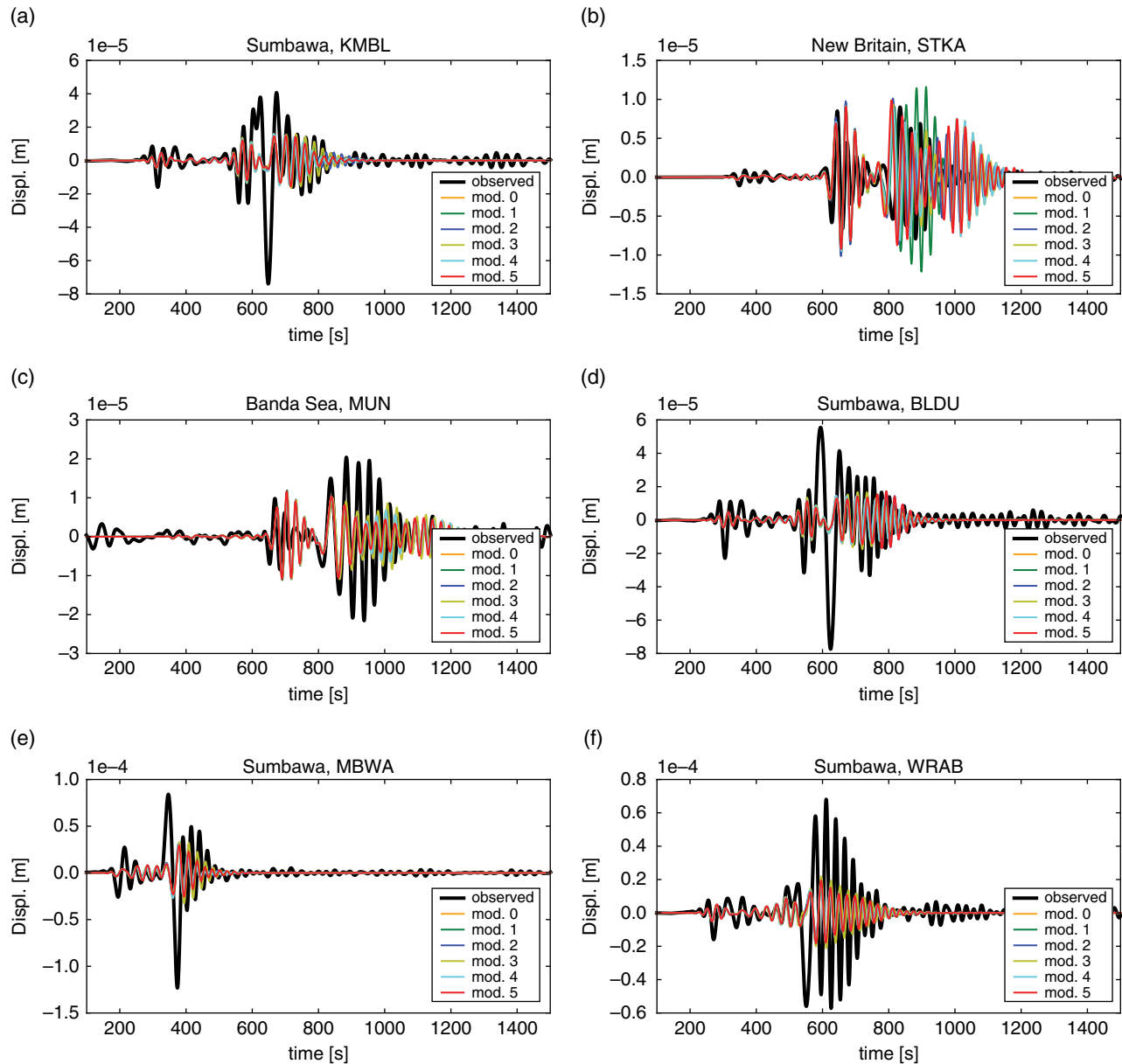


Figure 11.13 Seismograms (vertical component) computed from six regional Australian tomography models (mod. 0–5) from *Khan et al.* [2013], and compared with observed seismograms (“observed”) at a minimum period of 20 s. Instrument response was removed and original waveforms were filtered according to the source time spectrum, defined by four corner frequencies: 0.002, 0.005, 0.03, and 0.05 Hz. The title above each subplot designates the name of the event (e.g., Sumbawa) followed by the name of the seismic station (e.g., KMBL). For geographical information on station and event location see Figure 11.6.

11.4. SUMMARY REMARKS

In this study we have described a methodology to estimate Earth’s mantle composition and thermal state directly from geophysical data using a joint geophysical–thermodynamical approach. To connect geophysical observables (here in the form of seismic waveforms) with mantle temperature and composition, we rely on a self-consistent thermodynamic modeling scheme of

mantle mineral phase equilibria that depends only on composition, temperature, and pressure. What underlies the procedure is a large body of mineral physics-related data that derives from many experimental measurements and supplemented with results from first-principles calculations (e.g., see *Stixrude and Lithgow-Bertelloni* [2011]). In this manner we produce profiles of physical properties to obtain models of mantle conditions that simultaneously combine features of both laboratory and

geophysical data. An obvious advantage of the thermodynamic approach is that geophysical–petrological knowledge of, for example, location, size, and sharpness of mantle discontinuities is an inherent part of the data that would otherwise be difficult to resolve.

Increasing effort is being spent in trying to unravel the physical causes of the observed velocity variations that are seen in seismic tomography images. There is a growing consensus that the cause of the imaged wave-speed anomalies not only relates to variations in temperature, but also bears a strong compositional component. However, separation of thermal and chemical effects from seismic wave speeds alone is difficult and is further complicated by the general insensitivity of seismic wave speeds to the density contrasts that are ultimately responsible for driving mantle convection. Thus, placing better constraints on the density structure is key to improve our understanding of interior dynamical processes. However, density–velocity relationships are nonlinear and complex (e.g., see *Khan et al.* [2015]), as a result of which it is common practice to make use of ad hoc scaling relationships to link e.g., S-wave speed and density. In contrast, because composition and temperature act as fundamental parameters, the present set-up provides a natural means of determining all properties and their variations simultaneously and obviates the need for scaling relationships. For example, electrical conductivity, can enhance pictures of mineral composition and density in mantle models (e.g., see *Khan et al.* [2015]).

In summary, interpretation of the anomalies that are being uncovered at increasingly finer scales (e.g., see *Ritsema et al.* [2011] and *Schaeffer and Lebedev* [2013]) with a view to placing constraints on Earth's bulk composition and thermal state and ultimately its origin and evolution, is very likely not possible from a single vantage point. It requires integrated multidisciplinary efforts where data and models from a broad range of disciplines (e.g., geophysics, petrology, geochemistry, mineralogy, and geology where possible) are jointly processed. The foundations and tools for such interdisciplinary approaches already exist and it is not without reason that an increasing effort toward integrated studies is being undertaken given the potential improvements over more traditional approaches (e.g., see *Fullea et al.* [2009], *Khan et al.* [2009], *Verhoeven et al.* [2009], *Fullea et al.* [2012], *Khan and Shankland* [2012], *Afonso et al.* [2013a,b], *Drilleau et al.* [2013], and *Khan et al.* [2015]).

APPENDIX A: THE INVERSE PROBLEM: MARKOV CHAIN MONTE CARLO METHODS

Here we briefly summarize the essentials of solving the inverse problem probabilistically. For more detailed discussions, the reader is referred to the contributions by

Mosegaard and Hansen [2016], *Hansen et al.* [2016], and *Bosch* [2016] in this volume.

11.A1. A Quick Look at the Probabilistic Approach

The framework that allows us to integrate thermodynamical computations with seismology is the probabilistic approach to inverse problem [*Mosegaard and Tarantola*, 1995]. In the probabilistic approach the target of the inversion is the posterior probability density function, which is given by [*Tarantola*, 2005]

$$\sigma_M(\mathbf{m}) = k \rho_M(\mathbf{m}) L(\mathbf{m}), \quad (11.A1)$$

where \mathbf{m} are model parameters, $\rho_M(\mathbf{m})$ the prior probability distribution, $L(\mathbf{m})$ the likelihood function, k a normalization constant, and $\sigma_M(\mathbf{m})$ the posterior probability distribution. The latter expresses the probability related to the space of all conceivable Earth models M . The prior represents the knowledge we have on model parameters independently of the observed data, whereas the likelihood function measures the degree of fit between calculated and observed data and requires computation of the forward model $g(\mathbf{m})$, which may consist of several steps as is the case here. The intention is not to obtain a single “best” fit model as solution to the inverse problem, but a collection of models from the posterior in order to address issues related to uncertainty, nonuniqueness, resolution, and, not least, to accommodate the nonlinearity of the forward model.

In general, prior information plays a fundamental role in solving the inverse problem; in some cases, the availability of information independent of observed data may strongly impact the feasibility of the inversion. Using complex a priori information adapted to a specific problem, including correlations among model parameters, can help make a Monte Carlo search more effective (see, e.g., *Zunino et al.* [2015]).

With the goal of characterizing the posterior distribution, we can employ the “Extended Metropolis algorithm” [*Mosegaard and Tarantola*, 1995] to sample $\sigma_M(\mathbf{m})$ and obtain a (possibly large) collection of models as solution. The drawback of this algorithm is that a very large number of iterations are usually required to sample the posterior, which grows considerably with the number of model parameters. Once the ensemble of solutions is obtained, we use the following relationship (thanks to the *importance sampling* property of the algorithm) to obtain information about Earth's interior, since the posterior collection of models represents the complete solution to the inverse problem:

$$\int_M \Phi(\mathbf{m}) \sigma_M(\mathbf{m}) d\mathbf{m} \approx \frac{1}{N} \sum_{i=1}^N \Phi(\mathbf{m}^{(i)}), \quad (11.A2)$$

where $\Phi(\mathbf{m})$ represents a specific feature of interest and N represents the number of posterior models.

11.A2. Data Uncertainty

Observed seismic measurements are affected by noise, which is formally included in the definition of the likelihood function. In case of Gaussian noise, the likelihood function takes the form

$$L(\mathbf{m}) = k \exp \left[-\frac{1}{2} (\mathbf{g}(\mathbf{m}) - \mathbf{d}_{obs})^T \mathbf{C}_D^{-1} (\mathbf{g}(\mathbf{m}) - \mathbf{d}_{obs}) \right], \quad (11.A3)$$

where \mathbf{C}_D is the covariance matrix, \mathbf{d}_{obs} the observed data, $\mathbf{g}(\mathbf{m})$ the forward model, and k a normalization constant. More generally, under Gaussian assumptions, the covariance matrix \mathbf{C}_D can be expanded to include, if available, any theoretical uncertainty, such that $\mathbf{C}_D = \mathbf{C}_d + \mathbf{C}_T$, where \mathbf{C}_d is the covariance of observed data and \mathbf{C}_T the covariance describing uncertainty of the various steps of the forward modeling scheme.

APPENDIX B: ANELASTICITY

In modeling attenuation we compute shear quality factor Q_S using the laboratory-based model suggested by *Jackson et al.* [2002] and employed in our previous work [*Khan et al.*, 2011]. Specifically, we compute Q_S using the following expression (e.g., see *Jackson et al.* [2002]):

$$Q_S = Q_0 \exp \left[\frac{\alpha (E_a + pV_a)}{RT} \right], \quad (11.B1)$$

where Q_0 is a constant, E_a the activation energy, V_a the activation volume, p the pressure, T the temperature, R the gas constant, and α an exponent, which has been determined experimentally to be between 0.15 and 0.25 (e.g., see *Jackson et al.* [2002]). The compressional quality factor is obtained from $Q_P^{-1} = (4V_S^2 / 3V_P^2) Q_S^{-1}$. Assuming Q to be weakly frequency dependent (described by α), anelastically corrected (anharmonic) S -wave velocities V_S can be obtained from the expression (e.g., see *Anderson* [1989])

$$V_S(p, T, C) = v_S(p, T, C) \left[1 - \frac{2Q_S^{-1}}{\tan(\alpha\pi/2)} \right], \quad (11.B2)$$

where v_S is isotropic anharmonic S -wave velocity as a function of p , T , and composition C obtained using Gibbs free energy minimization as explained in Section 11.2.1. Anelastic corrections to P -wave velocities V_P are obtained by simply substituting v_P and Q_P for v_S and Q_S in the above expression. Based on recent

measurements, more complex rheological models (e.g., Andrade, extended Burgers, pseudo-period) have been proposed (e.g., see *Jackson et al.* [2010], *McCarthy et al.* [2011], and *Takei et al.* [2014]), but were not considered.

APPENDIX C: ANISOTROPY

We make the assumption of transverse anisotropy (symmetry axis in vertical direction), in which case the number of independent parameters of the elastic tensor reduce to 5. For present purposes we use the following anisotropic parameters V_{SV} , V_{SH} , V_{PV} , V_{PH} , where the subscripts denote vertically (V) and horizontally (H) polarized S -waves and vertically and horizontally propagating P -waves, respectively. We further introduce the three anisotropy parameters ξ , ϕ , and η , which are related to V_{SV} , V_{SH} , V_{PV} , V_{PH} through

$$\xi = \frac{V_{SH}^2}{V_{SV}^2}, \quad \phi = \frac{V_{PV}^2}{V_{PH}^2}, \quad \eta = \frac{F}{A - 2L}, \quad (11.C1)$$

where ξ and ϕ quantify S - and P -wave anisotropy, respectively, η describes the dependence of velocity on the incidence angle of a propagating wave [*Dziewonski and Anderson*, 1981; *Anderson and Dziewonski*, 1982], and F , A , and L are three of the Love coefficients. Reparameterizing in terms of the Voigt average of isotropic P - and S -wave velocities [*Babuska and Cara* 1991], we obtain

$$V_P^2 = \frac{V_{PV}^2 + 4V_{PH}^2}{5} \quad (11.C2)$$

$$V_S^2 = \frac{2V_{SV}^2 + V_{SH}^2}{3}, \quad (11.C3)$$

where V_S^2 and V_P^2 are isotropic (anelastically corrected) P - and S -wave velocities, respectively.

Summarizing, from the set of parameters $\{V_P, V_S, \xi, \phi, \eta\}$, anisotropic velocities are computed using the above equations, which are subsequently employed to determine Love and Rayleigh-wave dispersion curves. Note that because surface-wave overtone data are considered, sensitivity includes both S - and P -wave velocity.

ACKNOWLEDGMENTS

We thank two reviewers for constructive comments which helped improve the clarity of the manuscript. This work was supported by Swiss National Science Foundation grant IZK0Z2_154511. Waveform data used in this study were obtained from the IRIS Data Management Center (<http://www.iris.edu>).

REFERENCES

- Afonso, J. C., J. Fullea, W. L. Griffin, Y. Yang, A. G. Jones, J. A. D. Connolly, and S. Y. O'Reilly (2013a), 3-D multiobservable probabilistic inversion for the compositional and thermal structure of the lithosphere and upper mantle. I: A priori petrological information and geophysical observables, *J. Geophys. Res. (Solid Earth)*, *118*, 2586–2617, doi:10.1002/jgrb.50124.
- Afonso, J. C., J. Fullea, Y. Yang, J. A. D. Connolly, and A. G. Jones (2013b), 3-D multi-observable probabilistic inversion for the compositional and thermal structure of the lithosphere and upper mantle. II: General methodology and resolution analysis, *J. Geophys. Res. (Solid Earth)*, *118*, 1650–1676, doi:10.1002/jgrb.50123.
- Afonso, J. C., M. Moorkamp, and J. Fullea (2016), Imaging the lithosphere and upper mantle: Where we are at and where we are going, in *Integrated Imaging of the Earth: Theory and Applications*, Geophysical Monograph 218, M. Moorkamp, P. Lelievre, N. Linde, and A. Khan, eds., AGU, published by John Wiley & Sons, Hoboken, NJ, pp. 191–218.
- Anderson, D. L. (1989), *Theory of the Earth*, Blackwell Scientific Publications, London.
- Anderson, D. L. (2007), *New Theory of the Earth*, Cambridge University Press, Cambridge, UK.
- Anderson, D. L., and A. M. Dziewonski (1982), Upper mantle anisotropy—Evidence from free oscillations, *Geophys. J.*, *69*, 383–404.
- Babuska, V., and M. Cara (1991), *Seismic Anisotropy in the Earth (Modern Approaches in Geophysics)*, Springer, New York.
- Backus, G. (1962), Long-wave elastic anisotropy produced by horizontal layering, *J. Geophys. Res.*, *67*(11), 4427–4440.
- Bassin, C., G. Laske, and G. Masters (2000), The current limits of resolution for surface wave tomography in North America, *EOS Trans., AGU*, *81*, F897.
- Berryman, J. G. (1995), Mixture theories for rock properties, in *Rock Physics and Phase Relations: A Handbook of Physical Constants*, AGU, Washington D.C., 205–228, doi:10.1029/RF003p0205.
- Bina, C. R. (1998), Free energy minimization by simulated annealing with applications to lithospheric slabs and mantle plumes, *Pure Appl. Geophys.*, *151*, 605–618, doi:10.1007/s000240050132.
- Bina, C. R., and G. Helffrich (1994), Phase transition Clapeyron slopes and transition zone seismic discontinuity topography, *J. Geophys. Res.*, *99*, 15,853, doi:10.1029/94JB00462.
- Birch, F. (1952), Elasticity and constitution of the Earth's interior, *J. Geophys. Res.*, *57*, 227–286, doi:10.1029/JZ057i002p00227.
- Bosch, M. (2016), Inference networks in earth models with multiple components and data, in *Integrated Imaging of the Earth: Theory and Applications*, Geophysical Monograph 218, M. Moorkamp, P. Lelievre, N. Linde, and A. Khan, eds., AGU, published by John Wiley & Sons, Hoboken, NJ, pp. 29–47.
- Brown, J. M., and T. J. Shankland (1981), Thermodynamic parameters in the Earth as determined from seismic profiles, *Geophys. J.*, *66*, 579–596, doi:10.1111/j.1365-246X.1981.tb04891.x.
- Cammarano, F., S. Goes, P. Vacher, and D. Giardini (2003), Inferring upper-mantle temperatures from seismic velocities, *Phys. Earth Planet. Interiors*, *138*, 197–222, doi:10.1016/S0031-9201(03)00156-0.
- Cammarano, F., S. Goes, A. Deuss, and D. Giardini (2005), Is a pyrolytic adiabatic mantle compatible with seismic data?, *Earth Planet. Sci. Lett.*, *232*(3–4), 227–243, doi:10.1016/j.epsl.2005.01.031.
- Cammarano, F., B. Romanowicz, L. Stixrude, C. Lithgow-Bertelloni, and W. Xu (2009), Inferring the thermochemical structure of the upper mantle from seismic data, *Geophys. J. Int.*, *179*, 1169–1185, doi:10.1111/j.1365-246X.2009.04338.x.
- Cammarano, F., P. Tackley, and L. Boschi (2011), Seismic, petrological and geodynamical constraints on thermal and compositional structure of the upper mantle: Global thermochemical models, *Geophys. J. Int.*, *187*(3), 1301–1318.
- Capdeville, Y., L. Guillot, and J.-J. Marigo (2010a), 1-D non-periodic homogenization for the seismic wave equation, *Geophys. J. Int.*, *181*, 897–910, doi:10.1111/j.1365-246X.2010.04529.x.
- Capdeville, Y., L. Guillot, and J.-J. Marigo (2010b), 2-D non-periodic homogenization to upscale elastic media for P-SV waves, *Geophys. J. Int.*, *182*, 903–922, doi:10.1111/j.1365-246X.2010.04636.x.
- Capdeville, Y., É. Stutzmann, N. Wang, and J.-P. Montagner (2013), Residual homogenization for seismic forward and inverse problems in layered media, *Geophys. J. Int.*, *194*(1), 470–487.
- Capdeville, Y., M. Zhao, and P. Cupillard (2015), Fast Fourier homogenization for elastic wave propagation in complex media, *Wave Motion*, *54*, 170–186, doi:10.1016/j.wavemoti.2014.12.006.
- Chen, M., and Q. Shao (1998), Monte Carlo estimation of bayesian credible and hpd intervals, *J. Comput. Graph. Stat.*, *8*, 69–92.
- Cobden, L., S. Goes, F. Cammarano, and J. A. D. Connolly (2008), Thermochemical interpretation of one-dimensional seismic reference models for the upper mantle: Evidence for bias due to heterogeneity, *Geophys. J. Int.*, *175*, 627–648, doi:10.1111/j.1365-246X.2008.03903.x.
- Connolly, J. (2005), Computation of phase equilibria by linear programming: A tool for geodynamic modeling and its application to subduction zone decarbonation, *Earth and Planet. Sci. Lett.*, *236*(1), 524–541.
- Connolly, J. A. D. (2009), The geodynamic equation of state: What and how, *Geochem. Geophys., Geosyst.*, *10*, Q10014, doi:10.1029/2009GC002540.
- Connolly, J. A. D., and D. M. Kerrick (2002), Metamorphic controls on seismic velocity of subducted oceanic crust at 100–250 km depth, *Earth Planet. Sci. Lett.*, *204*, 61–74, doi:10.1016/S0012-821X(02)00957-3.
- Cupillard, P., Capdeville, Y. and Botella, A. (2015) Homogenization of 3d geological models for seismic wave propagation, in *SEG Technical Program Expanded Abstracts*, pp. 3656–3660.
- Cupillard, P., E. Delavaud, G. Burgos, G. Festa, J.-P. Vilotte, Y. Capdeville, and J.-P. Montagner (2012), RegSEM: A versatile code based on the spectral element method to compute seismic wave propagation at the regional scale, *Geophys. J. Int.*, *188*(3), 1203–1220.

- da Silva, C. R. S., R. M. Wentzcovitch, A. Patel, G. D. Price, and S. I. Karato (2000), The composition and geotherm of the lower mantle: constraints from the elasticity of silicate perovskite, *Physics Earth Planet. Interiors*, *118*, 103–109, doi:10.1016/S0031-9201(99)00133-8.
- Dahlen, F., S.-H. Hung, and G. Nolet (2000), Frechet kernels for finite-frequency traveltimes—I. Theory, *Geophys. J. Int.*, *141*, 157–174.
- Deschamps, F., R. Snieder, and J. Trampert (2001), The relative density-to-shear velocity scaling in the uppermost mantle, *Physics Earth Planet. Int.*, *124*, 193–212, doi:10.1016/S0031-9201(01)00199-6.
- Dobson, D. P., and J. P. Brodholt (2000), The electrical conductivity and thermal profile of the Earth's mid-mantle, *Geophys. Res. Lett.*, *27*, 2325–2328, doi:10.1029/1999GL008409.
- Drilleau, M., É. Beucler, A. Mocquet, O. Verhoeven, G. Moëbs, G. Burgos, J.-P. Montagner, and P. Vacher (2013), A Bayesian approach to infer radial models of temperature and anisotropy in the transition zone from surface wave dispersion curves, *Geophys. J. Int.*, *195*, 1165–1183, doi:10.1093/gji/ggt284.
- Dziewonski, A. M., and D. L. Anderson (1981), Preliminary reference Earth model, *Phys. Earth Planet. Interiors*, *25*, 297–356, doi:10.1016/0031-9201(81)90046-7.
- Dziewonski, A. M., T.-A. Chou, and J. H. Woodhouse (1981), Determination of earthquake source parameters from waveform data for studies of global and regional seismicity, *J. Geophys. Res.*, *86*, 2825–2852, doi:10.1029/JB086iB04p02825.
- Ekström, G., M. Nettles, and A. M. Dziewoński (2012), The global CMT project 2004–2010: Centroid-moment tensors for 13,017 earthquakes, *Phys. Earth Planet. Interiors*, *200*, 1–9, doi:10.1016/j.pepi.2012.04.002.
- Emry, E., A. Nyblade, J. Julià, S. Anandakrishnan, R. Aster, D. Wiens, A. Huerta, and T. Wilson (2015), The mantle transition zone beneath west antarctica: Seismic evidence for hydration and thermal upwellings, *Geochem., Geophys., Geosyst.*, *16*, 40–58.
- Fabrichnaya, O. (1999), The phase relations in the feo-mgo-al₂o₃-sio₂ system: Assessment of thermodynamic properties and phase equilibria at pressures up to 30 {GPa}, *Calphad*, *23*(1), 19–67, doi:10.1016/S0364-5916(99)00013-9.
- Fichtner, A., H. Igel, H.-P. Bunge, and B. Kennett (2009), Simulation and inversion of seismic wave propagation on continental scales based on a spectral-element method, *J. Numer. Anal., Indust. Appl. Math.*, *4*, 11–22.
- Fichtner, A., B. L. N. Kennett, H. Igel, and H.-P. Bunge (2010), Full waveform tomography for radially anisotropic structure: New insights into present and past states of the Australasian upper mantle, *Earth Planet. Sci. Lett.*, *290*, 270–280, doi:10.1016/j.epsl.2009.12.003.
- Fishwick, S., and N. Rawlinson (2012), 3-D structure of the Australian lithosphere from evolving seismic datasets, *Aust. J. Earth Sci.*, *59*, 809–826, doi:10.1080/08120099.2012.702319.
- Forte, A. M., and H. C. Perry (2000), Geodynamic evidence for a chemically depleted continental tectosphere, *Science*, *290*(5498), 1940–1944.
- Fullea, J., J. C. Afonso, J. A. D. Connolly, M. Fernández, D. Garca-Castellanos, and H. Zeyen (2009), LitMod3D: An interactive 3-D software to model the thermal, compositional, density, seismological, and rheological structure of the lithosphere and sublithospheric upper mantle, *Geochem., Geophys., Geosyst.*, *10*, Q08019, doi:10.1029/2009GC002391.
- Fullea, J., M. R. Muller, and A. G. Jones (2011), Electrical conductivity of continental lithospheric mantle from integrated geophysical and petrological modeling: Application to the Kaapvaal Craton and Rehoboth Terrane, southern Africa, *J. Geophys. Res. (Solid Earth)*, *116*(B15), B10202, doi:10.1029/2011JB008544.
- Fullea, J., S. Lebedev, M. R. Agius, A. G. Jones, and J. C. Afonso (2012), Lithospheric structure in the Baikal-central Mongolia region from integrated geophysical–petrological inversion of surface-wave data and topographic elevation, *Geochem., Geophys., Geosyst.*, *13*, Q0AK09, doi:10.1029/2012GC004138.
- Goes, S., R. Govers, and P. Vacher (2000), Shallow mantle temperatures under Europe from P and S wave tomography, *J. Geophys. Res.*, *105*, 11,153, doi:10.1029/1999JB900300.
- Goes, S., F. Cammarano, and U. Hansen (2004), Synthetic seismic signature of thermal mantle plumes, *Earth Planet. Sci. Lett.*, *218*, 403–419, doi:10.1016/S0012-821X(03)00680-0.
- Goes, S., F. J. Simons, and K. Yoshizawa (2005), Seismic constraints on temperature of the Australian uppermost mantle, *Earth Planet. Sci. Lett.*, *236*(1), 227–237.
- Guéguen, Y., and P. Victor (1994), *Introduction to the Physics of Rocks*, Princeton University Press, Princeton, NJ.
- Guillot, L., Y. Capdeville, and J. Marigo (2010), 2-D non-periodic homogenization of the elastic wave equation: SH case, *Geophys. J. Int.*, *182*, 1438–1454, doi:10.1111/j.1365-246X.2010.04688.x.
- Hacker, B. R., G. A. Abers, and S. M. Peacock (2003), Subduction factory 1. Theoretical mineralogy, densities, seismic wave speeds, and H₂O contents, *J. Geophys. Res. (Solid Earth)*, *108*, 2029, doi:10.1029/2001JB001127.
- Hansen, T. M., K. S. Cordua, A. Zunino, and K. Mosegaard (2015), Probabilistic integration of geo-information, in *Integrated Imaging of the Earth: Theory and Applications*, Geophysical Monograph 218, M. Moorkamp, P. Lelievre, N. Linde, and A. Khan, eds., AGU, published by John Wiley & Sons, Hoboken, NJ, pp. 93–116.
- Hashin, Z., and S. Shtrikman (1963), A variational approach to the theory of the elastic behaviour of multiphase materials, *J. Mech. Phys. Solids*, *11*(2), 127–140.
- Helffrich, G. (2000), Topography of the transition zone seismic discontinuities, *Rev. Geophys.*, *38*, 141–158, doi:10.1029/1999RG000060.
- Helffrich, G. R., and B. J. Wood (2001), The earth's mantle, *Nature*, *412*(6846), 501–507.
- Hill, R. (1952), The elastic behaviour of a crystalline aggregate, *Proc. Phys. Soc. A*, *65*, 349–354, doi:10.1088/0370-1298/65/5/307.
- Hofmann, A. (1997), Mantle geochemistry: The message from oceanic volcanism, *Nature*, *385*(6613), 219–229.
- Holland, T. J. B., and R. Powell (1998), An internally consistent thermodynamic data set for phases of petrological interest, *J. Metamorph. Geol.*, *16*(3), 309–343.
- Irifune, T. (1994), Absence of an aluminous phase in the upper part of the Earth's lower mantle, *Nature*, *370*, 131–133, doi:10.1038/370131a0.
- Ishii, M., and J. Tromp (2004), Constraining large-scale mantle heterogeneity using mantle and inner-core sensitive normal modes, *Phys. Earth Planet. Interiors*, *146*(1), 113–124.

- Jackson, I. (1998), Elasticity, composition and temperature of the Earth's lower mantle: A reappraisal, *Geophys. J. Int.*, *134*, 291–311, doi:10.1046/j.1365-246X.1998.00560.x.
- Jackson, I., J. D. Fitz Gerald, U. H. Faul, and B. H. Tan (2002), Grain-size-sensitive seismic wave attenuation in polycrystalline olivine, *J. Geophys. Res. (Solid Earth)*, *107*, 2360, doi:10.1029/2001JB001225.
- Jackson, I., U. H. Faul, D. Suetsugu, C. Bina, T. Inoue, and M. Jellinek (2010), Grainsize-sensitive viscoelastic relaxation in olivine: Towards a robust laboratory-based model for seismological application, *Phys. Earth Planet. Interiors*, *183*, 151–163, doi:10.1016/j.pepi.2010.09.005.
- Jones, A. G., R. L. Evans, and D. W. Eaton (2009), Velocity–conductivity relationships for mantle mineral assemblages in Archean cratonic lithosphere based on a review of laboratory data and Hashin–Shtrikman extremal bounds, *Lithos*, *109*, 131–143, doi:10.1016/j.lithos.2008.10.014.
- Kaban, M. K., M. Tesauero, W. D. Mooney, and S. A. P. L. Cloetingh (2014), Density, temperature, and composition of the North American lithosphere—New insights from a joint analysis of seismic, gravity, and mineral physics data: 1. Density structure of the crust and upper mantle, *Geochem., Geophys., Geosyst.*, *15*, 4781–4807, doi:10.1002/2014GC005483.
- Karato, S. (2013), *Physics and Chemistry of the Deep Earth*, Wiley-Blackwell, Hoboken, NJ.
- Käufel, P., A. Fichtner, and H. Igel (2013), Probabilistic full waveform inversion based on tectonic regionalization – development and application to the Australian upper mantle, *Geophys. J. Int.*, *193*, 437–451, doi:10.1093/gji/ggs131.
- Kennett, B., S. Widiyantoro, and R. van der Hilst (1998), Joint seismic tomography for bulk sound and shear wave speed in the earth's mantle, *J. Geophys. Res. Solid Earth (1978–2012)*, *103*(B6), 12,469–12,493.
- Khan, A., and F. Deschamps, eds. (2015), *The Earth's Heterogeneous Mantle—A Geophysical, Geodynamical, and Geochemical Perspective*, Springer Geophysics, New York.
- Khan, A., and T. J. Shankland (2012), A geophysical perspective on mantle water content and melting: Inverting electromagnetic sounding data using laboratory-based electrical conductivity profiles, *Earth Planet. Sci. Lett.*, *317*, 27–43, doi:10.1016/j.epsl.2011.11.031.
- Khan, A., J. A. D. Connolly, and N. Olsen (2006), Constraining the composition and thermal state of the mantle beneath Europe from inversion of long-period electromagnetic sounding data, *Journal of Geophysical Research (Solid Earth)*, *111*(B10), B10102, doi:10.1029/2006JB004270.
- Khan, A., J. A. D. Connolly, J. Maclennan, and K. Mosegaard (2007), Joint inversion of seismic and gravity data for lunar composition and thermal state, *Geophys. J. Int.*, *168*, 243–258, doi:10.1111/j.1365-246X.2006.03200.x.
- Khan, A., L. Boschi, and J. A. D. Connolly (2009), On mantle chemical and thermal heterogeneities and anisotropy as mapped by inversion of global surface wave data, *J. Geophys. Res. (Solid Earth)*, *114*, B09305, doi:10.1029/2009JB006399.
- Khan, A., A. Zunino, and F. Deschamps (2011), The thermochemical and physical structure beneath the North American continent from Bayesian inversion of surface-wave phase velocities, *J. Geophys. Res. (Solid Earth)*, *116*, B09304, doi:10.1029/2011JB008380.
- Khan, A., A. Zunino, and F. Deschamps (2013), Upper mantle compositional variations and discontinuity topography imaged beneath Australia from Bayesian inversion of surface-wave phase velocities and thermochemical modeling, *J. Geophys. Res. Solid Earth*, *118*(10), 5285–5306.
- Khan, A., S. Koch, T. J. Shankland, A. Zunino, and J. A. D. Connolly (2015), Relationships between seismic wave-speed, density, and electrical conductivity beneath Australia from seismology, mineralogy, and laboratory-based conductivity profiles, in *The Earth's Heterogeneous Mantle—A Geophysical, Geodynamical, and Geochemical Perspective*, A. Khan and F. D., eds., Springer Geophysics, New York.
- Komatitsch, D., and J.-P. Vilotte (1998), The spectral element method: An efficient tool to simulate the seismic response of 2d and 3d geological structures, *Bull. Seismol. Soc. Am.*, *88*(2), 368–392.
- Komatitsch, D., J. Ritsema, and J. Tromp (2002), The spectral-element method, *Beowulf computing, and global seismology*, *Science*, *298*, 1737–1742, doi:10.1126/science.1076024.
- Koyama, T., A. Khan, and A. Kuvshinov (2014), Three-dimensional electrical conductivity structure beneath Australia from inversion of geomagnetic observatory data: Evidence for lateral variations in transition-zone temperature, water content and melt, *Geophys. J. Int.*, *196*, 1330–1350, doi:10.1093/gji/ggt455.
- Kuo, C., and B. Romanowicz (2002), On the resolution of density anomalies in the Earth's mantle using spectral fitting of normal-mode data, *Geophys. J. Int.*, *150*, 162–179, doi:10.1046/j.1365-246X.2002.01698.x.
- Kuskov, O. L., and A. B. Panferov (1991), Phase diagrams of the FeO–MgO–SiO₂ system and the structure of the mantle discontinuities, *Phys. Chem. Minerals*, *17*, 642–653, doi:10.1007/BF00203845.
- Kuskov, O. L., V. A. Kronrod, and A. A. Prokofyev (2011), Thermal structure and thickness of the lithospheric mantle underlying the Siberian Craton from the kraton and kimberlit superlong seismic profiles, *Izv. Phys. Solid Earth*, *47*, 155–175, doi:10.1134/S1069351310111011.
- Kuskov, O. L., V. A. Kronrod, A. A. Prokofyev, and N. I. Pavlenkova (2014), Thermochemical structure of the lithospheric mantle underneath the Siberian craton inferred from long-range seismic profiles, *Tectonophysics*, *615*, 154–166, doi:10.1016/j.tecto.2014.01.006.
- Lee, S.-H., J. Rhie, Y. Park, and K.-H. Kim (2014), Topography of the 410 and 660 km discontinuities beneath the Korean Peninsula and southwestern Japan using teleseismic receiver functions, *J. Geophys. Res. (Solid Earth)*, *119*, 7245–7257, doi:10.1002/2014JB011149.
- Lekic, V., and B. Romanowicz (2011), Tectonic regionalization without a priori information: A cluster analysis of upper mantle tomography, *Earth Planet. Sci. Lett.*, *308*, 151–160, doi:10.1016/j.epsl.2011.05.050.
- Liu, Q., and Y. J. Gu (2012), Seismic imaging: From classical to adjoint tomography, *Tectonophysics*, *566*, 31–66, doi:10.1016/j.tecto.2012.07.006.
- Marton, F. C., and R. E. Cohen (2002), Constraints on lower mantle composition from molecular dynamics simulations of MgSiO₃ perovskite, *Phys. Earth Planet. Interiors*, *134*, 239–252, doi:10.1016/S0031-9201(02)00189-9.

- Matas, J., J. Bass, Y. Ricard, E. Mattern, and M. S. T. Bukowinski (2007), On the bulk composition of the lower mantle: Predictions and limitations from generalized inversion of radial seismic profiles, *Geophys. J. Int.*, *170*, 764–780, doi:10.1111/j.1365-246X.2007.03454.x.
- Mattern, E., J. Matas, Y. Ricard, and J. Bass (2005), Lower mantle composition and temperature from mineral physics and thermodynamic modelling, *Geophys. J. Int.*, *160*, 973–990, doi:10.1111/j.1365-246X.2004.02549.x.
- McCarthy, C., Y. Takei, and T. Hiraga (2011), Experimental study of attenuation and dispersion over a broad frequency range: 2. The universal scaling of polycrystalline materials, *J. Geophys. Res. (Solid Earth)*, *116*, B09207, doi:10.1029/2011JB008384.
- Montelli, R., G. Nolet, F. A. Dahlen, G. Masters, E. R. Engdahl, and S.-H. Hung (2004), Finite-frequency tomography reveals a variety of plumes in the mantle, *Science*, *303*, 338–343, doi:10.1126/science.1092485.
- Mosca, I., L. Cobden, A. Deuss, J. Ritsema, and J. Trampert (2012), Seismic and mineralogical structures of the lower mantle from probabilistic tomography, *J. Geophys. Res. Solid Earth*, *117*, B06304.
- Mosegaard, K., and T. M. Hansen (2016), Inverse methods: Problem formulation and probabilistic solutions, in *Integrated Imaging of the Earth: Theory and Applications*, Geophysical Monograph 218, M. Moorkamp, P. Lelievre, N. Linde, and A. Khan, eds., AGU, published by John Wiley & Sons, Hoboken, NJ, pp. 9–27.
- Mosegaard, K., and A. Tarantola (1995), Monte Carlo sampling of solutions to inverse problems, *J. Geophys. Res. Solid Earth (1978–2012)*, *100*(B7), 12,431–12,447.
- Nissen-Meyer, T., M. van Driel, S. C. Stähler, K. Hosseini, S. Hempel, L. Auer, A. Colombi, and A. Fournier (2014), AxiSEM: Broadband 3-D seismic wavefields in axisymmetric media, *Solid Earth*, *5*, 425–445, doi:10.5194/se-5-425-2014.
- Piazzoni, A. S., G. Steinle-Neumann, H.-P. Bunge, and D. Dolejš (2007), A mineralogical model for density and elasticity of the Earth's mantle, *Geochem. Geophys. Geosyst.*, *8*, Q11010, doi:10.1029/2007GC001697.
- Resovsky, J. S., and M. H. Ritzwoller (1999), A degree 8 mantle shear velocity model from normal mode observations below 3 mHz, *J. Geophys. Res.*, *104*, 993–1014, doi:10.1029/1998JB900025.
- Ricard, Y., E. Mattern, and J. Matas (2005), Synthetic tomographic images of slabs from mineral physics, *Washington DC Am. Geophys. Union Geophys. Monogr. Ser.*, *160*, 283–300, doi:10.1029/160GM17.
- Ritsema, J., W. Xu, L. Stixrude, and C. Lithgow-Bertelloni (2009), Estimates of the transition zone temperature in a mechanically mixed upper mantle, *Earth Planet. Sci. Lett.*, *277*(1–2), 244–252, doi:10.1016/j.epsl.2008.10.024.
- Ritsema, J., A. Deuss, H. J. van Heijst, and J. H. Woodhouse (2011), S40RTS: A degree-40 shear-velocity model for the mantle from new Rayleigh wave dispersion, teleseismic travel-time and normal-mode splitting function measurements, *Geophys. J. Int.*, *184*, 1223–1236, doi:10.1111/j.1365-246X.2010.04884.x.
- Romanowicz, B. (2001), Can we resolve 3D density heterogeneity in the lower mantle?, *J. Geophys. Res.*, *28*, 1107–1110, doi:10.1029/2000GL012278.
- Saxena, S. K., and G. Eriksson (1983), Low- to medium-temperature phase equilibria in a gas of solar composition, *Earth Planet. Sci. Lett.*, *65*, 7–16, doi:10.1016/0012-821X(83)90185-1.
- Schaeffer, A. J., and S. Lebedev (2013), Global shear speed structure of the upper mantle and transition zone, *Geophys. J. Int.*, *194*, 417–449, doi:10.1093/gji/ggt095.
- Schmandt, B., S. D. Jacobsen, T. W. Becker, Z. Liu, and K. G. Dueker (2014), Dehydration melting at the top of the lower mantle, *Science*, *344*, 1265–1268, doi:10.1126/science.1253358.
- Schmerr, N. (2015), Imaging mantle heterogeneity with upper mantle seismic discontinuities, in *The Earth's Heterogeneous Mantle—A Geophysical, Geodynamical, and Geochemical Perspective*, A. Khan and F. Deschamps, eds., Springer Geophysics, New York.
- Schmerr, N., and E. Garnero (2006), Investigation of upper mantle discontinuity structure beneath the central Pacific using SS precursors, *J. Geophys. Res. (Solid Earth)*, *111*, B08305, doi:10.1029/2005JB004197.
- Schuberth, B. S. A., C. Zanolli, and G. Nolet (2012), Synthetic seismograms for a synthetic earth: long-period p- and s-wave traveltimes variations can be explained by temperature alone, *Geophys. J. Int.*, *188*(3), 1393–1412, doi:10.1111/j.1365-246X.2011.05333.x.
- Shapiro, N., and M. Ritzwoller (2004), Thermodynamic constraints on seismic inversions, *Geophys. J. Int.*, *157*(3), 1175–1188.
- Simmons, N. A., A. M. Forte, L. Boschi, and S. P. Grand (2010), GyPSuM: A joint tomographic model of mantle density and seismic wave speeds, *J. Geophys. Res. (Solid Earth)*, *115*(B14), B12310, doi:10.1029/2010JB007631.
- Sobolev, S. V., and A. Y. Babeyko (1994), Modeling of mineralogical composition, density and elastic wave velocities in anhydrous magmatic rocks, *Surv. Geophys.*, *15*, 515–544, doi:10.1007/BF00690173.
- Stixrude, L., and R. Jeanloz (2007), *Constraints on Seismic Models from Other Disciplines—Constraints from Mineral Physics on Seismological Models*, Vol. I, Elsevier, Amsterdam, Chapter 22, pp. 775–803.
- Stixrude, L., and C. Lithgow-Bertelloni (2005a), Thermodynamics of mantle minerals—I. Physical properties, *Geophys. J. Int.*, *162*(2), 610–632.
- Stixrude, L., and C. Lithgow-Bertelloni (2005b), Mineralogy and elasticity of the oceanic upper mantle: Origin of the low-velocity zone, *J. Geophys. Res. (Solid Earth)*, *110*, B03204, doi:10.1029/2004JB002965.
- Stixrude, L., and C. Lithgow-Bertelloni (2007), Influence of phase transformations on lateral heterogeneity and dynamics in Earth's mantle, *Earth Planet. Sci. Lett.*, *263*, 45–55, doi:10.1016/j.epsl.2007.08.027.
- Stixrude, L., and C. Lithgow-Bertelloni (2011), Thermodynamics of mantle minerals—II. Phase equilibria, *Geophys. J. Int.*, *184*(3), 1180–1213.
- Tackley, P. J., S. Xie, T. Nakagawa, and J. W. Hernlund (2005), Numerical and laboratory studies of mantle convection: Philosophy, accomplishments, and thermochemical structure and evolution, *Washington DC Am. Geophys. Union Geophys. Monogr. Ser.*, *160*, 83–99, doi:10.1029/160GM07.

- Takei, Y., F. Karasawa, and H. Yamauchi (2014), Temperature, grain size, and chemical controls on polycrystal anelasticity over a broad frequency range extending into the seismic range, *J. Geophys. Res. (Solid Earth)*, *119*, 5414–5443, doi:10.1002/2014JB011146.
- Takeuchi, N., H. Kawakatsu, S. Tanaka, M. Obayashi, Y. J. Chen, J. Ning, S. P. Grand, F. Niu, J. Ni, R. Iritani, K. Idehara, and T. Tonegawa (2014), Upper mantle tomography in the northwestern Pacific region using triplicated P waves, *J. Geophys. Res. (Solid Earth)*, *119*, 7667–7685, doi:10.1002/2014JB011161.
- Tarantola, A. (2005), *Inverse Problem Theory and Methods for Model Parameter Estimation*, SIAM, Philadelphia.
- Tauzin, B., E. Debayle, and G. Wittlinger (2008), The mantle transition zone as seen by global Pds phases: No clear evidence for a thin transition zone beneath hotspots, *J. Geophys. Res. (Solid Earth)*, *113*, B08309, doi:10.1029/2007JB005364.
- Tauzin, B., R. D. van der Hilst, G. Wittlinger, and Y. Ricard (2013), Multiple transition zone seismic discontinuities and low velocity layers below western United States, *J. Geophys. Res. (Solid Earth)*, *118*, 2307–2322, doi:10.1002/jgrb.50182.
- Thompson, D. A., J. O. S. Hammond, J.-M. Kendall, G. W. Stuart, G. R. Helffrich, D. Keir, A. Ayele, and B. Goitom (2015), Hydrous upwelling across the mantle transition zone beneath the Afar Triple Junction, *Geochem., Geophys., Geosyst.*, *16*, 834–846, doi:10.1002/2014GC005648.
- Trampert, J., F. Deschamps, J. Resovsky, and D. Yuen (2004), Probabilistic tomography maps chemical heterogeneities throughout the lower mantle, *Science*, *306*(5697), 853–856.
- Turcotte, D. L., and G. Schubert (2002), *Geodynamics*, 2nd ed., Cambridge University Press, Cambridge, UK, doi:10.2277/0521661862.
- Vacher, P., A. Mocquet, and C. Sotin (1998), Computation of seismic profiles from mineral physics: the importance of the non-olivine components for explaining the 660 km depth discontinuity, *Phys. Earth Planet. Interiors*, *106*, 275–298, doi:10.1016/S0031-9201(98)00076-4.
- van der Hilst, R. D., J. D. Bass, J. Matas, and J. E. Trampert (2005), Earth's deep mantle: Structure, composition, and evolution, *AGU, Geophys. Monogr. Ser.*, *160*, 344 pp., doi:10.1029/GM160.
- van Gerven, L., F. Deschamps, and R. D. van der Hilst (2004), Geophysical evidence for chemical variations in the Australian Continental Mantle, *Geophys. Res. Lett.*, *31*, L17607, doi:10.1029/2004GL020307.
- Verhoeven, O., A. Mocquet, P. Vacher, A. Rivoldini, M. Menvielle, P.-A. Arrial, G. Choblet, P. Tarits, V. Dehant, and T. van Hoolst (2009), Constraints on thermal state and composition of the Earth's lower mantle from electromagnetic impedances and seismic data, *J. Geophys. Res. (Solid Earth)*, *114*, B03302, doi:10.1029/2008JB005678.
- Visser, K., J. Trampert, and B. L. N. Kennett (2008), Global anisotropic phase velocity maps for higher mode Love and Rayleigh waves, *Geophys. J. Int.*, *172*, 1016–1032, doi:10.1111/j.1365-246X.2007.03685.x.
- Watt, J. P., G. F. Davies, and R. J. O'Connell (1976), The elastic properties of composite materials, *Rev. Geophys. Space Phys.*, *14*, 541, doi:10.1029/RG014i004p00541.
- Wood, B. J., and J. R. Holloway (1984), A thermodynamic model for subsolidus equilibria in the system CaO–MgO–Al₂O₃–SiO₂, *Geochim. Cosmochim. Acta*, *48*, 159–176, doi:10.1016/0016-7037(84)90358-2.
- Xu, W., C. Lithgow-Bertelloni, L. Stixrude, and J. Ritsema (2008), The effect of bulk composition and temperature on mantle seismic structure, *Earth Planet. Sci. Lett.*, *275*, 70–79, doi:10.1016/j.epsl.2008.08.012.
- Xu, Y., T. J. Shankland, and B. T. Poe (2000), Laboratory-based electrical conductivity in the Earth's mantle, *J. Geophys. Res.*, *105*, 27,865, doi:10.1029/2000JB900299.
- Zunino, A., J. A. D. Connolly, and A. Khan (2011), Precalculated phase equilibrium models for geophysical properties of the crust and mantle as a function of composition, *Geochem., Geophys., Geosyst.*, *12*, Q04001, doi:10.1029/2010GC003304.
- Zunino, A., K. Mosegaard, K. Lange, Y. Melnikova, and T. Mejer Hansen (2015), Monte Carlo reservoir analysis combining seismic reflection data and informed priors, *Geophysics*, *80*, 31, doi:10.1190/geo2014-0052.1.